AUTOMATED GLIAL IMAGE ANALYSIS AND BIOINFORMATICS

A Dissertation
Presented to
The Academic Faculty

By

Tiffany Ly

In Partial Fulfillment
of the Requirements for the Degree
Doctor of Philosophy in the
Charles L. Brown School of Electrical and Computer Engineering

Advisor: Dr. Scott T. Acton
Virginia Image and Video Analysis Lab
University of Virginia

June 22, 2021

ABSTRACT

The interaction between the central nervous system (CNS) and immune system is crucial in maintaining homeostasis. Scientists have recently realized the extreme significance of the role of CNS immune cells after injury, in aging, and in neurodegenerative disease. Morphological changes of microglia cells, which are immune cells in the brain, can reveal the state of the CNS. However, manual quantification of these complex morphologies is tedious, error-prone, and potentially biased. The primary objective of this thesis is to provide an automatic image-based engineering solution to study *microglia structure and motion.*

We propose a fully automatic system for quantifying 3D images of glial morphology over time to produce accurate image-based bioinformatics in naive and diseased settings. The quantification of morphology requires acquiring consistent digital reconstructions of the morphology, which is a challenging open problem in bioimage analysis. First, we describe an automatic 3D segmentation algorithm, called the coupled Tubularity flow field-Blob flow field (Tuff-Bff) for images of microglia. Tuff-Bff introduces a geometric deformable model designed to simultaneously reconstruct the large cell body and thin tubular processes. Our method found a 20% performance increase against state-of-the-art segmentation methods on a dataset of 3D images of microglia even in images with intensity heterogeneity throughout the object. The coupled Tuff-Bff segmentation results also yielded 40% improvement in accuracy for the ramification index of the processes, which reveals the efficacy of our method.

We also provide a methodology, called *Hieroglyph*, for consistent reconstruction of morphology over time using a novel hierarchical graph matching of *glyphs*, a term we use to describe the graph theoretic tree representation of glia. Our temporal graph representation possesses information about the connections between the paths of a cell and node in the path. This information is used to track the digital reconstruction at subsequent time frames. These temporal glyphs contain all the complex morphological data for a glia in space and time.

Hieroglyph yielded a 21% performance increase compared to the state-of-the-art automatic skeleton reconstruction methods and outperforms the state of the art in different measures of consistency on datasets of 3D images of microglia.

To improve glial tracing we introduce C3VFC (Critical points on constrained Concentric Circles using Vector Field Convolution), which utilizes vector field convolution for detection and labeling of multiple cells in 3D images over time, leading to multi-object reconstruction. The C3VFC reconstruction results yielded more than 50% improvement on the next best performing tracing method. C3VFC achieved the highest accuracy scores, in relation to the baseline results, in four of the five different measures: entire structure average, the average bi-directional entire structure average, the different structure average, and the percentage of different structure.

Finally, we show that our automatic digital reconstruction system can provide a set of image-based bioinformatic measures for glia morphology and motility, including the volume covered, path length, path velocity, and bifurcation angle. We use the results from the three reconstruction algorithms to determine useful quantitative measurements to determine surveillance and ramification of microglia in naive, diseased, and injured animal models.

ACKNOWLEDGEMENTS

I would like to thank my advisor, Dr. Scott Acton, for his mentorship, support, and guidance throughout my research and career. It has been a tough path towards this PhD but I am deeply grateful for Dr. Acton's advice and encouragement. My sincerest thanks to my committee members Dr. Tajie Harris, Dr. Daniel Weller, Dr. Tom Fletcher and Dr. Gustavo Rhode for their time and guidance on this thesis.

I am incredibly grateful for my friends and lab mates in the VIVA laboratory. I appreciate VIVA's collaborative environment and have learned so much from the lab. My sincere thanks to Dr. Rituparna Sarkar, Dr. Nazia Tabassum, Dr. Jie Wang, and Dr. Tamal Batabyal for your help and advice throughout my research.

My parents and brother have been remarkably supportive throughout my life. I am immensely thankful for my friends and UVA family who have continuously supported and encouraged me throughout my PhD.

TABLE OF CONTENTS

LIST OF FIGURES

LIST OF TABLES

CHAPTER 1
INTRODUCTION

Recently, scientists have found that the central nervous system (CNS) and the immune system are not two isolated systems, but rather connected systems [1, 2]. More specifically, neurons in the CNS communicate with microglia (the tissue-resident immune cells of the brain parenchyma), which play an active role in brain homeostasis. The advancements made in the recent studies of microglia have shifted our understanding of the impact of microglia not only in development, but also their role in injury, disease, and aging [3, 4, 5, 6]. The morphological changes of microglia are directly associated with functional roles in the normal and the pathological CNS.

Glia are cells in the central and peripheral nervous system. Microglia are a type of glial cell located in the CNS, or brain and spinal cord, that are the resident macrophages. This means that microglia are the primary immune cells in the CNS that play a critical role during brain development (embryonic and postnatal stages) and maintaining homeostasis. Microglia originate in the mesodermal region but migrate to and disseminate throughout the brain parenchyma. During development, microglia are pruning neuron synapses to decide which connections stay. Microglia processes (thin 'legs' that extend from the cell body, or soma) are constantly in motion for surveillance to maintain homeostasis, or stable conditions. These processes allow microglia to sense and respond rapidly to their environment. They phagocyte, or absorb and engulf, damaged neuron synapses, plaques, dead or dying cells, or secrete cytotoxic substances that can kill bacteria or other unwanted agents [7, 8, 9, 10, 11, 12].

Figure 1.1 depicts microglia in two different states: resting and activated. When microglia processes are ramified it is termed "resting" microglia state. However, in response to disease, microglia become "activated" where they transition from a highly ramified state to

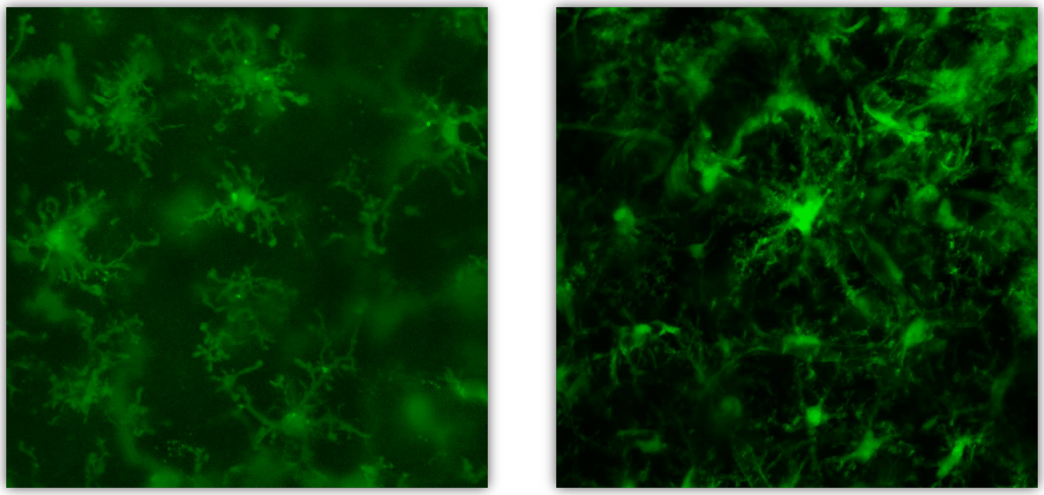

Figure 1.1: Resting microglia (right) and activated microglia (left)

a less ramified, amoeboid state [13, 14]. During brain injury and disease, for example, the continual movement of microglia processes is altered as microglia retract their processes and take on a more amoeboid morphology. Such morphological changes may play a role in the progression of neurodegenerative diseases, such as Parkinson's disease, multiple sclerosis, and Alzheimer's disease. Microglia are highly activated during the presence of these diseases and scientists are trying to understand the role of microglia in these settings. Changes in microglia morphology have been linked and proven to be associated with neurodegenerative diseases and infections. Quantifying microglia morphology and activity can help scientists understand how they are sampling their environment. Staining and imaging microglia can help quantify microliga length over time, the volume it covers over time, and other morphological informatics. This thesis meets a major need of the immunology and neuroscience communities; namely, it provides a toolbox of image-based bioinformatics for glia.

1.1 Understanding the "third element" through imaging

We credit the founder of modern neuroscience to Santiago Ramon y Cajal, who (with Camillo Golgi) won the Nobel Prize for their work on "the structure of the nervous system."

Ramon y Cajal illustrated the precise network of neurons in which he later hypothesized the *neuron doctrine.* This doctrine described the nervous system made up of individual cells, or neurons, connected by small contact zones.

However, the history of image processing and microglia perhaps dates back to 1880 when Franz Nissl developed Nissl staining which gave scientists the ability to view neural cells, including microglia. Nissl then described microglia in their resting state, activated, and bipolar, rod state.

A student of Ramón y Cajal, Nicolás Achúcarro also visualized the rod shaped cells that Nissl had described in the brain of rabbits that had been infected by rabies. With his tannin and amoniacal silver nitrate staining method, he was able to image these cells, which he called granuloadipose cells. Achúcarro hypothesized that the role of these cells were to phagocytize, or ingest, damaged neurons. He also described the cell's rod shape morphology and movement was related to degenerated neurons. He further hypothesized that glial cell dysfunction could cause brain disease which is still being researched today [15]. These findings are imperative to the little we know about glia today. Ramon y Cajal followed Achúcarro to study and attempt to visualize neuroglia with his sublimated gold chloride method. However, he could only clearly image astrocytes and named the unknown neuroglia the "third element" in the nervous system.

Achúcarro's student, Pío del Río-Hortega continued the research on these cells and developed a novel imaging technique in which he stained the brain with ammoniacal silver carbonate method. This stain allowed him to clearly visualize and illustrate glial cells. In these illustrations, he clearly labeled and differentiated three glial cells in the brain: astrocytes, oligiodendrocytes, and microglia. With this eminent staining method, Río-Hortega was able to study microglia and define microglia in different settings. First, he contradicted Cajal's presumptions of the 'third element'. He found that microglia originated from the mesoderm and are related to leukyocytes, whereas oligiodendrites are different and more similar to astrocytes. Microglia actively phagocyte dendritic spines and cells

during brain development. He also studied microglia cells during brain damage in which he saw their morphological changes and activate, noting that they proliferate and phagocytose debris in pathological settings [16, 15].

Even a century ago, we witnessed the great impact of novel imaging techniques on how much or little is known about a single cell. Despite these findings, microglia still remains the least understood cell in the nervous system today. Microglia had been viewed as "resting" in a healthy brain until real time *in-vivo* imaging using two-photon microscopy revealed that its fine processes are highly motile during homeostasis.

The bipolar, rod morphology visualized by Nissl in 1899 was seen apparent in neurological disorders and sleep disorders by Spielmeyer in 1922 [17]. Since then, microglia have been linked to brain injury, Alzheimer's disease, Parkinson's disease, Huntington's disease, and other neurodegenerative diseases [18, 19, 20, 21]

Microglia morphology are seen to change from ramified to amoeboid and bipolar, rod states in certain disease settings. It has been a century since these morphological findings appeared, yet the microglia's functional roles in adulthood and during neuronal injuries is still being uncovered.

The morphological changes of microglia are directly associated with their functional roles in normal and pathological central nervous systems. A resting microglia is ramified during homeostasis, while a microglia changes to amoeboid shape or bipolar, rod shape during an injury, depending on the stimulus. Further, microglia morphology is even more dynamic, where its other shapes are not yet categorized [14].

1.2 Background on Microglia Segmentation and Tracing

The role of microglia in neurological diseases, brain injury, and aging is still being studied and uncovered, but we do know that glia are highly activated in such cases. Scientists are trying to understand microglia by studying their gene expression and their morphology in different settings. Currently, most microglia image analysis is done by hand where scientists

manually trace the processes. With a high-throughput of images, we may be able to reveal a quantitative model of morphological differences, but manual analysis is tedious and not feasible. *In this thesis, we want to automate the quantification of glial morphology and motion via image analysis.*

1.2.1 Background on Segmentation

"One picture is worth a thousand words." Fred R. Barnard popularized this quote, in which he depicted the use of images in the advertising industry. An image holds a lot of information. Yet, what is labeled as useful information, is relative to the application. In the realm of digital image processing, it is important to extract useful information from an image in order to further understand the image. That could entail extracting certain objects or areas within an image with similar characteristics, or features. Segmentation is an important technique within digital image processing that partitions an image into segments; it is commonly used to separate or find boundaries of an object. Popular segmentation applications include the domains of cell and biological segmentation, medical imaging, handwritten or text detection in natural language processing, object detection and recognition, and much more.

Perhaps one of the earliest and still most common segmentation technique is thresholding. The thresholding technique places pixel values above a specific threshold pixel value into the foreground and labels pixel values below the threshold value as the background. Thresholding works best when there is high contrast between the foreground and background pixels of interest. The threshold value can be determined manually by a human examining the image histogram or automatically using an algorithm that determines this threshold. One of the first automatic segmentation techniques was developed by Noboyuki Otsu which automatically determines the threshold value. The Otsu thresholding technique is a non-parametric algorithm that detects and separates peaks, or threshold value, in the gray level histogram of an image, thus separating the foreground and background pixels [22]. This algorithm is still widely used due to its simplicity, since it does not require

pre-determined parameters. However, this technique fails when there is high signal-to-noise ratio and inhomogeneity within the objects in an image, which lead to mis-classified pixels. Thus, this method may require pre-processing techniques, such as image enhancement and denoising. In some images, such as in biological imaging or in low contrast images, these pre-processing tasks can be very difficult. There are other thresholding algorithms that discriminate multiple classes, but in general thresholding algorithms require a "clean" image. However, variants of thresholding techniques are widely used by scientists because of their simplicity and computational efficiency. Other classical segmentation techniques include pixel-based methods (morphological operations, connected component analysis), edge-based methods, region-based methods (watershed), model-based methods, and graph cuts.

1.2.2 Segmentation and analysis of microglia and similar biological images

It is difficult to find a generalizable segmentation technique that provides accurate results for every kind of image. There are many variants within an image that can affect the segmentation result. For example, the morphology and complexity of the object, and the image quality can affect the segmentation result of differing segmentation techniques. For example, for our images of microglia, a thresholding technique would capture background noise and would not capture all the processes due to intensity inhomogeniety, as explained in Section 1.4.

It is helpful to look at previous research on segmentation techniques for images similar to microglia. Since microglia is an immune cell in the brain, it is also helpful to look at research done for other astrocytes and neurons. Other images with similar morphology include retinal image data. These images also have a region with complex branching coming out of it. Neuronal images, in particular, have been studied since the early 1900s when Santiago Ramón y Cajal presented the idea that a neuron's shape, connectivity, and network were directly correlated to its function and the brain's functions [23]. This idea carried

throughout the studies within neuroscience. Since then engineers have developed a myriad of algorithms to help analyze cell morphology and function.

Biological reconstructions could refer to segmentation or tracing, which are sometimes used interchangeably. Segmentation refers to separating the foreground from the background by finding the boundary of the object. Tracing refers to finding the centerline or medial axis of an object. For microglia images, the soma is usually represented by its center of mass. However, more recent tracing includes the entire segmentation of the soma in the tracing for quantification accuracy.

Morphological reconstruction is an important technique for the analysis of cell morphology. Yet even in NeuroMorpho.org, the largest curated inventory of publicly accessible 3D neuronal reconstructions, less than 5% of the reconstructions are traced in a semi-automatic fashion, while the remainder are manually traced [24]. The complexity of glia morphology makes it difficult to automate the analysis of glia motility. Existing studies have manually traced glial images or used heuristic image processing methods to measure process length, extension, and retraction over time [25, 26, 27, 28]. Nimmerjahn *et al.* manually traced the ends of microglia processes to get a rough estimation of the velocity of length change and drew out microglia for other measurements [25]. This manual method does not give accurate measurements for the fine processes and is not feasible for high throughput data. Others quantified microglia size and processes movement by thresholding the foreground and background [27], manually outlining the cell, and manually counting primary branches using ImageJ software (National Institutes of Health) [29].

Researchers have developed automatic image analysis methods involving the reconstruction of skeletons of the microglia processes [30, 31]. In [30], the skeletonization was semi-automatic in that the user went through many pre-processing tasks in ImageJ before achieving a 2D skeleton. However, 2D skeletonization loses information since the skeletons may overlap in the z direction, as shown in our experimental results. ProMoIJ achieves an automatic reconstruction of a 3D skeleton of glia, which is then used to analyze microglia

motility [31]. However, the skeletonization is not accomplished for the entire cell; rather, each process of the glial cell is manually selected by the user. Furthermore, the user must define a set of parameters to heuristically pre-process the image and create a skeleton. This reconstruction of the processes over time is manually assisted.

An automated segmentation effort for microglia images was reported by Madry *et al.* in which Vaa3D software is used to trace microglia [12] and by Ding *et al.*'s framework that uses variational methods to segment multiple microglia in a 2D image with lower magnification [32]. Numerous state-of-the-art microglia segmentation algorithms use variations of thresholding techniques to automatically segment microglia, including multi-level thresholding, preprocessing by denoising, or classic Otsu-thresholding [33, 34, 35, 36, 37]. Thresholding is the oldest automatic segmentation technique that is favorable because of its simplicity, but it does not result in accurate reconstruction results due to microscopy imaging challenges, such as low contrast, background clutter, and intensity inhomogeneity. Microglia have very thin processes that are not fully captured by these thresholding methods. To this date, numerous highly cited works in the literature still use thresholded microglia images for their quantitative analysis [36, 37]. As discussed later, imaging microglia from healthy and infected mice with multiphoton microscopy results in images with varying intensity contrast throughout the cell which makes it difficult to threshold and separate the object from the background, in which state of the art segmentation techniques can not capture. However, some methods do use thresholding to acquire a more accurate result using minimum spanning trees [38, 39]. In [28], the authors also used a different thresholding method to segment the microglia images. They also automatically acquired a skeleton of the microglia image in three steps: calculating a distance map from a binary mask, breaking up the distance map with the watershed algorithm, then connecting broken segments with a straight line using a graph and minimum spanning tree. While these papers found a sufficient method to segment and analyze microglia morphology, the reconstruction methodology required excellent raw image quality, yet the reconstruction results were still noisy and did

not capture all of the foreground object.

In [40, 41], the researchers developed an algorithm that automatically skeletonized and segmented 3D images of microglia. They were able to find the centerline of the processes using an active contour method, which they then used to reconstruct the cell. However, this algorithm still only processes one image at a time. It is imperative to have a consistent reconstruction over time in order to attain an accurate analysis of the image data. Glial cells make up 60% of the brain parenchyma yet there are over 300,000 papers in the literature on neuronal reconstruction and very limited on microglia reconstruction. A challenge we face in this thesis is finding sufficient state-of-the-art algorithms related to microglia reconstruction to compare to. Microglia image reconstruction is a widely open problem.

1.3 Imaging

For part of this thesis, we use image datasets collected by the Harris lab at the University of Virginia. These datasets are 3D temporal images of microglia, or 4D images, in mouse models. We have datasets of microglia of healthy mice and those of mice that have been infected by the *Toxoplasma gondii* parasite. As described above, we do see that, in the infected mice, some microglia soma are ruptured into an amoeboid-like state and the processes decrease in activity. We use these datasets to automate the image analysis of glia in order to quantify these differences in morphology during activity.

The dataset consists of 3D images of microglia from mice using multiphoton microscopy. To label microglia in the mouse brain we used mice with an inducible cre recombinase under the control of the CX3CR1 promoter crossed to the Ai6 fluorescent reporter mouse (Jackson Laboratories, Bar Harbor, ME) to generate CX3CR1creERT2/+ X Ai6ZsGreen [42, 43]. At post-natal day (P23) 23, mice were given 10uL/g body weight of a 20mg/mL Tamoxifen (Sigma) solution in corn oil to induce recombination of the floxed stop codon leading to ZsGreen expression in microglia. All procedures adhered to guidelines of the Institutional Animal Care and Use Committee (ACUC) at the University of Virginia. Microglia of adult

mice (7-10 weeks old) were imaged using a Leica TCS SP8 multiphoton microscopy system equipped with a Coherent Chameleon Ti:Sapphire laser and a 25x 0.95 NA immersion lens. ZsGreen was excited with a wavelength of 880 nm.

The 3D movies of microglia were imaged over 20 minutes with z-stacks taken at one minute intervals, containing single or multiple microglia per field of view. Some of the images were cropped from a larger field of view containing about 10 different cells and two images were imaged from a zoomed in view of one individual cell. The images ranged from a horizontal pixel width of .01 um and a vertical pixel width of .01 um to horizontal pixel width of .2 um and a vertical pixel width of .2 um. In the 3D images, there is variation in intensity contrast throughout the cell, non-structural noise, and fluorescence bleeding through the z-stack due to the lengthy imaging technique, which makes it difficult to visualize and process. The images were pre-processed using histogram equalization which increased the intensity throughout the cell but further increased noise in the background.

We also used image datasets collected by the Eyo Lab at the University of Virginia. The datasets contain 3D multicellular images of microglia and blood vessels. Some of the datasets attain images with burn spots to show the motility and morphology changes. The multi-cellular dataset consists of 3D images of microglia from living mice using *in vivo* multiphoton microscopy. Heterozygous GFP reporter mice expressing GFP under control of the fractalkine receptor promoter ($Cx3cr1^{GFP/+}$) were used for the imaging studies. Wild-type C57/B6 mice were crossed with $CX3CR1^{GFP/GFP}$ mice from Jackson labs (Stock No. 005582) to generate $Cx3cr1^{GFP/+}$ for all experiments to visualize microglia.

These multi-cellular 3D movies of microglia were imaged over 16 minutes taken at one minute intervals, containing single or multiple microglia per field of view. The 3D images were $1024 \times 1024 \times 61$ pixels where the x-y frame size was $295\mu m \times 295\mu m$. The z-stacks' depth was taken in $1\mu m$ intervals. There are about 5-18 different cells in each multi-cellular video dataset. The images were taken in different settings that would significantly vary the movement and morphology between the videos.

All procedures adhered to guidelines of the Institutional Animal Care and Use Committee (ACUC) at the University of Virginia. Microglia of adult mice (7-10 weeks old) were imaged using a Leica TCS SP8 multiphoton microscopy system equipped with a Coherent Chameleon Ti:Sapphire laser and a 25x 0.95 NA immersion lens. ZsGreen was excited with a wavelength of 880 nm.

1.4 Difficulties in Automating the Analysis of these images

Two-photon microscopy is a popular image acquisition tool for imaging 3D live and thicker biological subjects. Two photon microscopy produces sharp images of an optical sectioned plane, without using a pinhole aperture (unlike confocal microscopy); rather using two photons with a longer wavelength than the emitted light. In contrast with conventional confocal microscopy, two-photon microscopy achieves less attenuation, or loss of intensity, as scattering within the subject decreases with excitation frequency.

Microglia imaging using *in vivo* two-photon microscopy still comes with challenges. Microscopy images often exhibit background noise and clutter resulting from non-microglia fluorescence or artifacts. The images may potentially have low contrast between the foreground and background. The processes or branches of the microglia are much smaller in radius compared to the soma, hence they have lower intensity than the soma does. There is also intensity inhomogeneity throughout the microglia processes meaning that the intensity varies along the processes, which would make it difficult to separate the foreground from the background. 3D imaging provides more information of the imaging subject in the z direction. This is advantageous for microglia since their processes extend out of the soma in multiple directions. However, part of the microglia could be out of the imaging field-of-view due to the complex nature of the processes or if the imaging cuts it off. Microglia in different settings have significantly different soma/process size, shape, and length which makes it difficult to use generalized segmentation and tracing techniques.

1.5 Objectives and Contributions

The **first** objective of this thesis is to create *an automatic segmentation algorithm for 3D glia images* in different settings. Segmentation helps to answer the important scientific question of how much volume are glia processes covering and their motility in different settings. With an increased high-throughput of 3D image data, automatic segmentation becomes a necessary task. We propose an automatic segmentation algorithm for 3D glial images that can capture the fine processes and soma of glia. Our coupled tubularity flow field (TuFF)-blob flow field (BFF) method evolves a level set towards the object boundary using the directional tubularity and blobness measure of 3D images.

The **second** objective is the *automatic reconstruction of morphology that is consistent over time*. The ramification and activity of glial processes changes in different settings and may be indicative of a homeostatic state or an unhealthy state. Thus, temporal image analysis is important for understanding cell function. Manually analyzing the morphology can become a difficult task, yet, current automatic morphology analysis methods cannot capture an accurate, consistent morphology. We propose an automatic method for the consistent morphology construction of 3D glia by using prior temporal information, called *Hieroglyph*. This is achieved by representing the glia as a graph network and splitting the branches into hierarchies. The 3D temporal skeletonization is then constructed by using the skeleton and glial graph information at the prior time frame to hierarchically track the movement of glia at the following time frames. We propose a second automatic tracing algorithm called *C3VFC* that uses **v**ector **f**ield **c**onvolution to find the **c**ritical points along the centerline of an object and trace paths that traverse back to the soma of every cell in an image. The solution provides detection and labeling of multiple cells in an image over time, leading to multi-object reconstruction. The reconstruction results can be used to extract bioinformatics from temporal data in different settings.

The **third** objective is to *quantify the differences in morphology and motility of glia in*

different settings. This aim integrates the tools we created for segmentation and morphology reconstruction to extract a set of bioinformatics. The segmentation algorithm from the first objective allows us to quantify 3D surveillance of the processes. The temporal graph information from the second objective gives us numerous quantification information, including path length, path velocity, the amount of extension and retraction, bifurcation angles, and the number of terminal nodes. From this information, our aim is to produce metrics that could differentiate and characterize glia in different settings. These metrics would help in making connections between morphology and function. This would be a significant contribution to the study of neurodegenerative disorders and diseases.

CHAPTER 2
SEGMENTATION

The goal of automating glial image analysis is to extract quantitative data from images to learn something about their morphology and motion. In such cases, we would want information about the activity of the processes which surveil the environment during homeostasis. From an image processing perspective, the most critical step in automatic digital reconstruction is segmentation. Segmentation is the separation of the foreground from the background, which in this case is separating the cell from the background. While there have been a multitude of segmentation techniques that have arisen for different problems, techniques geared towards biological image data still do not solve all segmentation needs and scientists must reconstruct their data manually. Often, rendered biological images have low contrast, intensity inhomogeneity, and disruptive background noise making it difficult for automatic reconstruction methods to produce a clean segmentation output.

In this chapter, we introduce an automatic segmentation algorithm specific to microglia called the coupled Tubularity flow field and Blob flow field (Tuff-Bff). Previous methods do not provide adequate results for microglia images. In Chapter 1, we outlined the challenges of microglia reconstruction and analysis. The coupled Tuff-Bff is a geometric active contour based method that segments both the processes and the soma of the microglia.

2.1 Background on Active Contours

An active contour, or snake, is a thin deformable model that is placed in an image where it will delineate towards the boundaries of desired objects. Active contour models are energy-based segmentation problems that maximize or minimize energy via an optimization technique. Geometric active contours are favored for biological image segmentation because of the ability to split and merge for ranges of topologies. Biological images tend to have

a multitude of objects with varying and complex morphologies. Microglia images, for example, can have soma and processes with varying soma sizes and shapes in different settings or even in a single frame of view. The goal of active contour model segmentation is to evolve an initial contour iteratively optimizing to get the boundary as close to an object as possible. Geometric active contours are implemented via a variational level set method. For a 2D curve, in a 2D image, think of a 3D topographical surface that is growing in a third dimension. This surface implicitly defines a curve or level set where the surface equation has a height of zero. So for a 3D image:

$$C = \{(x, y, z) : \phi(x, y, z, t) = 0\} \tag{2.1}$$

where C is the curve represented by all the points $x, y, z \in \Omega$. $\Omega \subset \mathbb{R}^3$ is the image domain for a 3D image. This representation of the curve, C, with the level set ϕ is implicit, which benefits topological activity of merging and splitting the level set. $\phi = 0$ at the object boundary, $\phi > 0$ inside the object boundary, and $\phi < 0$ outside of the object boundary. If we visualize the level set function as a surface, $\phi(x, y, z, t)$ is the height of the surface at time t. An energy functional is minimized when ϕ, the zero level set, reaches the object boundary. The active contour is updated by differentiating $\phi(x, y, z, t)$ with respect to time. The derivation can be found in [44]. For a general level set model, the active contour moves in a direction normal to the contour. Thus, the velocity (x_t, y_t, z_t) constrained by the normal direction gives us the curve motion equation, or the speed of the active surface:

$$F = (x_t, y_t, z_t) \cdot \mathbf{n} \tag{2.2}$$

for the unit normal **n**. The outward normal vector is:

$$\mathbf{n} = \frac{\nabla(x, y, z, t)}{|\nabla(x, y, z, t)|} \tag{2.3}$$

thus, the classic snake update equation is then:

$$\phi_t + F|\nabla(x, y, z, t)| = 0 \tag{2.4}$$

where $\phi_t = \dfrac{d\phi(x, y, z, t)}{dt}$. The goal of most of these active contour segmentation problems is to find a proper speed function, F, to control the evolution of the active contour towards the desired boundary.

2.2 Coupled Tubularity Flow-Field and Blob Flow Field

A flow-field technique is an approach to segmentation that uses a vector to extend the segmented region. Coupled TuFF-BFF is an automatic microglia segmentation algorithm that optimally combines the tubularity flow field technique (Tuff) [45] with a blob flow field (BFF) technique. The TuFF algorithm is specific to neuron dendritic trees because it only searches for tubular structures in an image. The fine processes of microglia do have tubular shapes, but the TuFF algorithm does not account for the microglia soma. Our coupled TuFF-BFF algorithm segments both the processes and soma while minimizing the overlap of their segmentation. Coupled TuFF-BFF is in the family of active contour models that pull a contour or snake towards the edges or lines of the object in an image [46, 47, 48, 49, 50, 51, 52]. The snake is evolved by minimizing an energy functional, $\varepsilon(\phi)$, that follows some constraints until it converges to the object boundary, or zero level set. ϕ is the level set function that is positive inside the zero level set and is negative on the outside.

TuFF [45] uses the tubular structure of the vessel-like objects to evolve a level set towards the objects boundary. The evolution of the contour relies on the tubular vector field of the image [48] which is attained by the orthonormal eigenvectors $\mathbf{e}_i(\mathbf{x})$, where $\mathbf{x}$ is the pixel position within the image domain Ω. The eigenvectors are ordered by increasing magnitude of the eigenvalues, $|\lambda_1| \leq |\lambda_2| \leq |\lambda_3| >> 0$. These eigenvalues are attained by computing the Hessian matrix of the Gaussian-smoothed image. The algorithm uses

Frangi's vessel enhancement technique[53] to distinguish and enhance tubular structures in an image by using a multiscale vesselness function according to the three directions of $\mathbf{e}_i(\mathbf{x})$. The segmentation is achieved by minimizing an energy functional $\varepsilon(\phi)$:

$$\varepsilon(\phi) = \varepsilon_{reg}(\phi) + \varepsilon_{evolve}(\phi) + \varepsilon_{attr}(\phi) \tag{2.5}$$

$$\varepsilon_{reg}(\phi) = v_1 \int_{\Omega} |\nabla H(\phi)| d\mathbf{x} \tag{2.6}$$

$$\varepsilon_{evolve}(\phi) = -\int_{\Omega} \sum_{i=1}^{d} \alpha_i \langle \mathbf{e}_i(\mathbf{x}), \mathbf{n}(\mathbf{x}) \rangle^2 H(\phi) d\mathbf{x} \tag{2.7}$$

where $\varepsilon(x)_{reg}$ is the smoothness energy, $\varepsilon(x)_{evolve}$ is the curve evolution energy, and $\varepsilon(x)_{attr}$ is the attraction energy. In Eq. 2.2, the smoothness weight, v_1, controls the smoothness of the level set curve. $\varepsilon(x)_{reg}$ constrains the length of the zero level set with the gradient of the Heaviside function in terms of ϕ. In Eq. 2.2, the vector $\mathbf{n}(\mathbf{x}) = \dfrac{\nabla\phi(\mathbf{x})}{|\nabla\phi(\mathbf{x})}$ is the outward normal to the zero level set of ϕ which effects the evolution along the vessel width. In the evolution energy d is the image dimension. Thus, for a 3D image, the axial vector component, $\mathbf{e}_1$ controls the curve evolution in the direction perpendicular to itself. Whereas, the orthogonal vector components, $\mathbf{e}_2$ and $\mathbf{e}_3 i$ also controls the curve evolution in the perpendicular direction to itself, normal to the vessel axis. α_i effects the curve evolution along the vessel width and axial direction. $\varepsilon_{attr}(\phi)$ is the attractive energy which uses the vector field to connect smaller disjoint fragments to larger fragments during the segmentation, as depicted in Figure 2.1. The energy functional, $\varepsilon(\phi)$, is minimized where ϕ is iteratively updated using gradient descent [45].

The effect of the axial and orthogonal components in the evolution energy functional in Eq. 2.2 are shown in Figure 2.2.

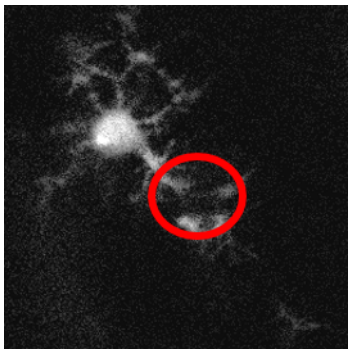

Figure 2.1: Original image may have disjoint segments.

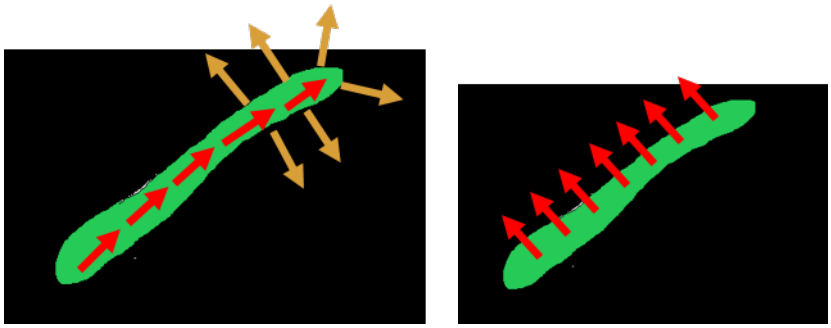

Figure 2.2: Axial vector flow field (left) and orthogonal vector flow field (right)

2.3 The Coupled Tubularity Flow Field and Blob Flow Field (Tuff-Bff)

Similar to the tubularity measure, the proposed method uses a blobness vector field in the algorithm to account for the soma of the cell. Since the soma and the processes have varying thickness, we scale the width of the Gaussian corresponding to their sizes, where the width of the soma is to be much larger than the width of the fine processes. The blobness measure is calculated by again ordering the eigenvalues of the Hessian matrix by increasing magnitudes, $|\lambda_1| \leq |\lambda_2| \leq |\lambda_3|$ to attain a structure that has high magnitude of λ in all three orthonormal directions [53, 54].

After computing the tubular and blobness information, the initial level set is attained from the 3D stack. The level set contours ϕ_1 to capture the processes and ϕ_2 to capture the soma are separately initialized by Otsu thresholding [22] the image's vessel- and blob-enhanced image. The processes and soma of microglia are simultaneously segmented by

	λ_1	λ_2	λ_3
Vesselness	Low	High	High
Blobness	High	High	High

Figure 2.3: Determining vesselness and blobness with Hessian analysis.

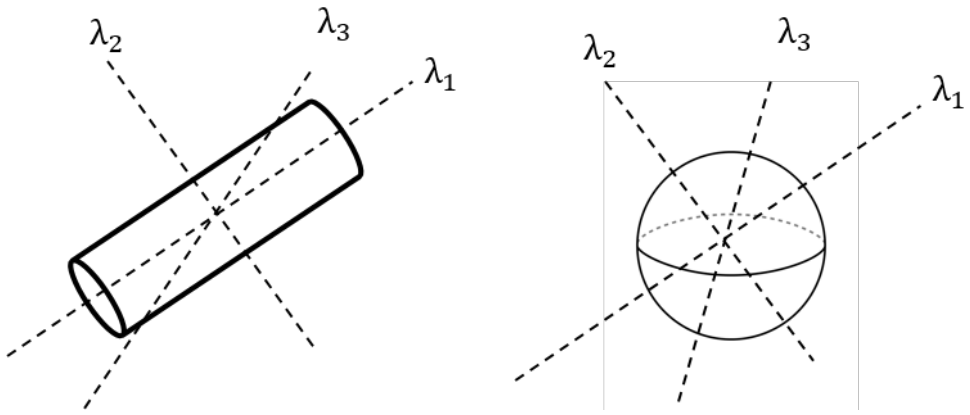

Figure 2.4: Eigenvalues magnitude in three directions.

evolving their level sets and minimizing their respective energy functionals, $\varepsilon_{TuFF}(\phi_1)$ and $\varepsilon_{BFF}(\phi_2)$:

$$\varepsilon_{TuFF}(\phi_1) = \varepsilon_{reg}(\phi_1) + \varepsilon_{evolve}(\phi_1) + \varepsilon_{attr}(\phi_1) + \varepsilon_{repel}(\phi_2) \tag{2.8}$$

$$\varepsilon_{BFF}(\phi_2) = \varepsilon_{reg}(\phi_2) + \varepsilon_{evolve}(\phi_2) + \varepsilon_{attr}(\phi_2) + \varepsilon_{repel}(\phi_1) \tag{2.9}$$

$$\varepsilon_{repel}(\phi_i) = \int_{\Omega} H(\phi_{TuFF})H(\phi_{BFF})dx \tag{2.10}$$

The evolution energy term, regulation energy term, and attraction energy terms were described above through Equations 2.2 and 2.2. The coupled Tuff-Bff algorithm contains ab additional repel term and two energy functionals, $\varepsilon_{TuFF}(\phi_1)$ and $\varepsilon_{BFF}(\phi_2)$, that controls the curve evolution for the tubular-like vessels and the blob-like soma, respectively. Although

the vesselness and blobness segmentations are separate, they are linked by using the result of both level sets in the $\varepsilon_{repel}(\phi)$ term. $\varepsilon_{repel}(\phi_i)$ penalizes the regions of overlap between the two level sets. The level set functions ϕ can be iteratively updated by solving $\frac{\partial \varepsilon}{\partial \phi}$ which, by the chain rule, can be solved with $\frac{\partial \phi}{\partial t}$, where *t* denotes each iteration[45]. We call this *F*, the velocity of the level set implementation:

$$F = \frac{\partial \phi_{reg}}{\partial t} + \alpha \frac{\partial \phi_{evolve}}{\partial t} + v_1 \frac{\partial \phi_{attr}}{\partial t} + r \frac{\partial \phi_{repel}}{\partial t} \tag{2.11}$$

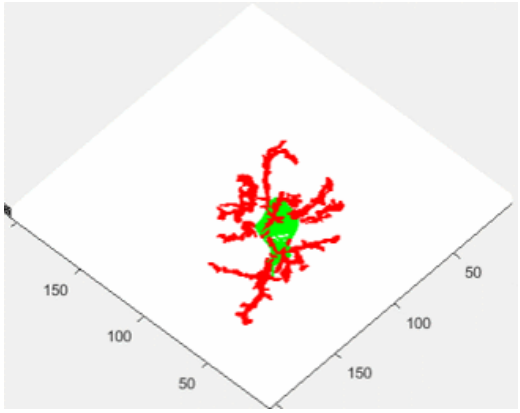

Figure 2.5: The soma and processes are separately yet simultaneously reconstructed.

The regions of overlap between both level sets are computed for $r\frac{\partial \phi_{repel}}{\partial t}$, where the repel term $r = 0$ when there is no overlap. This term changes the velocity, *F*, within the overlapping regions to repel away from their opposing level set ϕ. Thus, the repel force energy functional $\varepsilon_{repel}(\phi)$ minimizes the overlap between the segmentation of the processes and soma to attain a joint segmentation, as depicted in Figure 2.5.

2.4 Experimental Results and Analysis

The dataset consists of 3D images of microglia imaged from healthy mice brains using multi-photon microscopy, as explained in Section 1.3.

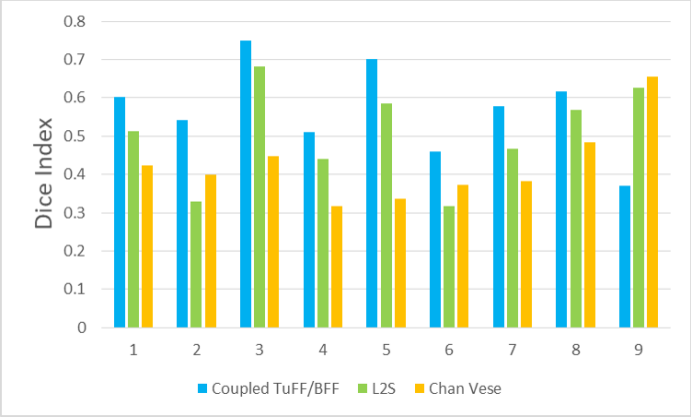

Figure 2.6: Dice index of the segmentation using Coupled TuFF-BFF, L2S[55], and Chan-Vese[56].

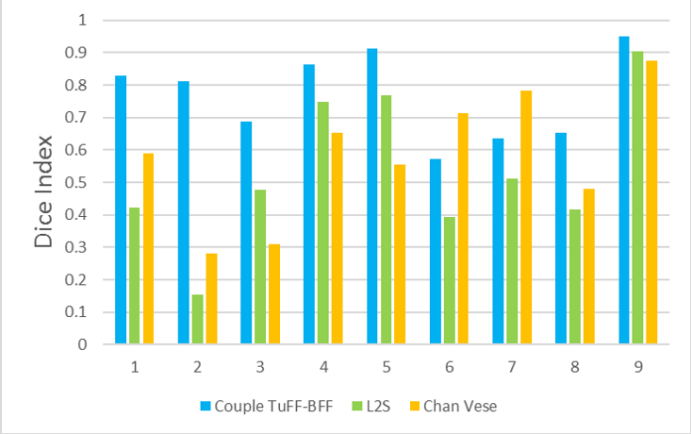

Figure 2.7: Dice index of surveyed area from the segmentation using Coupled TuFF-BFF, L2S[55], and Chan-Vese[56].

2.4.1 Performance evaluation

In our experiments, we compare the coupled TuFF-BFF microglia segmentation results with those given by L2S [55] and the Chan-Vese segmentation method [56]. The groundtruth in 3D was attained by manually tracing the object slice by slice from the z-stack. It must be noted that this was done by eye and could have some error. Figure 2.8 shows the visual comparison of the segmentation results for our dataset. Our result shown on the third column captures both the soma and processes. Figure 2.6 shows the Dice coefficient comparison of each segmentation method to the ground truth. Since the soma is much larger than the fine processes in the microglia, the processes have less volumetric impact on the similarity score. As explained in Section 1, segmenting the processes is important for quantifying the extension from the soma and its volume of surveillance. We use the Dice coefficient to quantitatively compare the ramification by taking the convex hull of the resulting segmentation. The Dice coefficient is a similarity measure that is computed using with $2 * \frac{|intersection(A,B)|}{(|A|+|B|)}$ where A is the ground truth and B is the compared image.

From Figure 2.7, the average Dice score for coupled TuFF-BFF was 0.77, compared to 0.53 for L2S [55] and 0.58 for Chan-Vese [56]. It must be noted that L2S required manual user initialization for each 2D image in the stack. While the Chan-Vese method has automatic seed selection, our coupled TuFF/BFF method was the only method that was a true 3D segmentation algorithm. L2S could not consistently capture the entire processes due to the intensity inhomogeneity throughout the object and background noise. The Chan-Vese segmentation could capture the extensions of the processes but did not work well with noise and attained false positives in the reconstruction. Since our method uses the tubular and blob information of the object to separate foreground and background, the segmentation only evolved within the object boundaries.

From the segmentation of microglia from 3D multiphoton images, we attained quantification of the ramification of the microglia processes using the index provided by Madry *et al.* The ramification index in Table 1 quantifies the extension of the processes from the

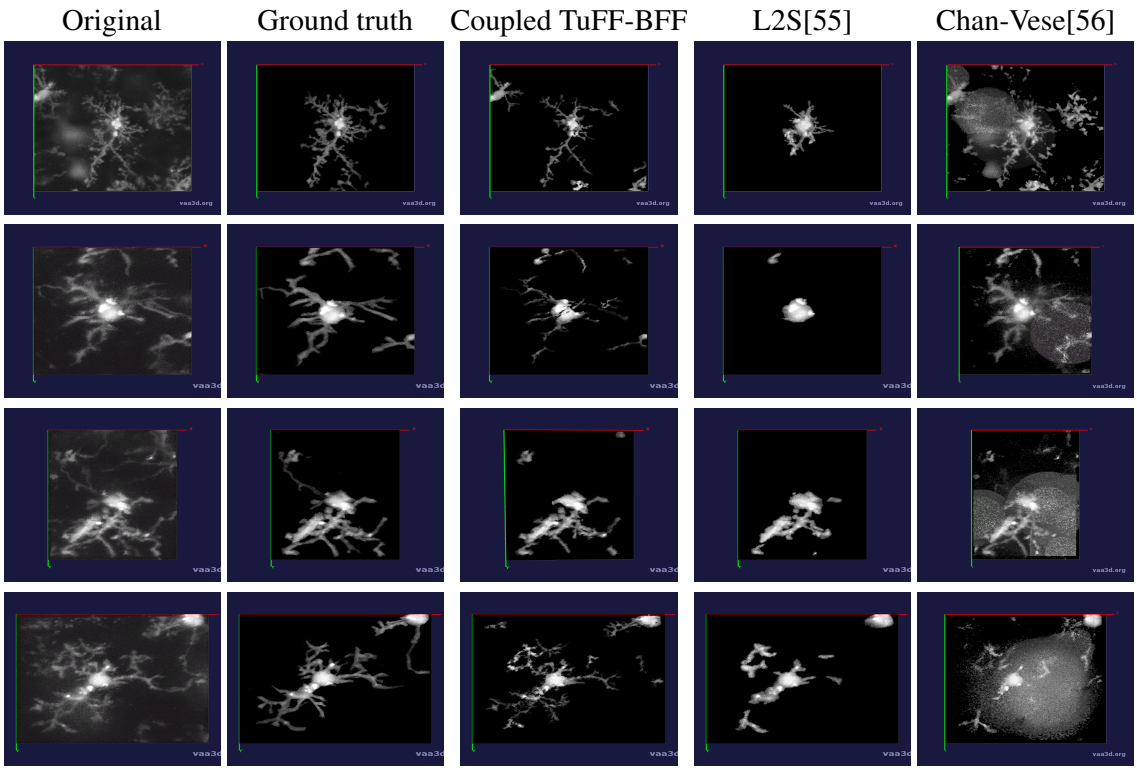

Figure 2.8: Segmentation results of 3D microglia images.

soma for each image. The ramification index of 1 is the soma with no ramification and a larger index denotes greater ramification. We compare the ramification index attained from the segmentation result from each method with that attained from the ground truth. The mean absolute error for coupled TuFF-BFF was 1.49 compared with 3.92 and 3.78 for L2S [55] and Chan-Vese [56], respectively. Our method appears to achieve the closest results to the ramification index of the ground truth which shows a more realistic application-based measure.

Table 1 Ramification Index

No.	groundtruth	TuFF-BFF	L2S	Chan-Vese
#1	8.88	7.88	4.0	7.46
#2	7.69	10.14	2.1	9.89
#3	6.54	5.98	4.34	8.76
#4	9.02	13.6	5.48	12.4
#5	6.44	7.22	5.26	18.3
#6	8.60	8.74	3.57	11.0
#7	9.09	7.70	4.78	12.86
#8	8.88	7.88	4.0	7.46
#9	11.18	12.7	7.56	16.48
MAE:	–	1.49	3.92	3.78

2.5 Discussion

In this section, we proposed an automated segmentation method, coupled TuFF-BFF, that segments microglia in 3D images. The method does not depend on prior image smoothing. Coupled TuFF-BFF was able to segment processes and soma from 3D images of microglia from the mouse brain. It was able to simultaneously capture the object of interest from images despite intensity inhomogeneity throughout the cell and background noise. While our method performed better than the state of the art, it could be further improved to attain a more accurate thickness of the cell and capture the low intensity areas of the branches. We plan to apply our method on images of microglia from mice in other states that significantly alters the microglia morphology. Another extension planned involves using coupled TuFF-BFF within existing cell tracking algorithms [49, 51, 52]. Future work relevant to this section will be briefly discussed later in Chapter 3 as it pertains to work in that chapter.

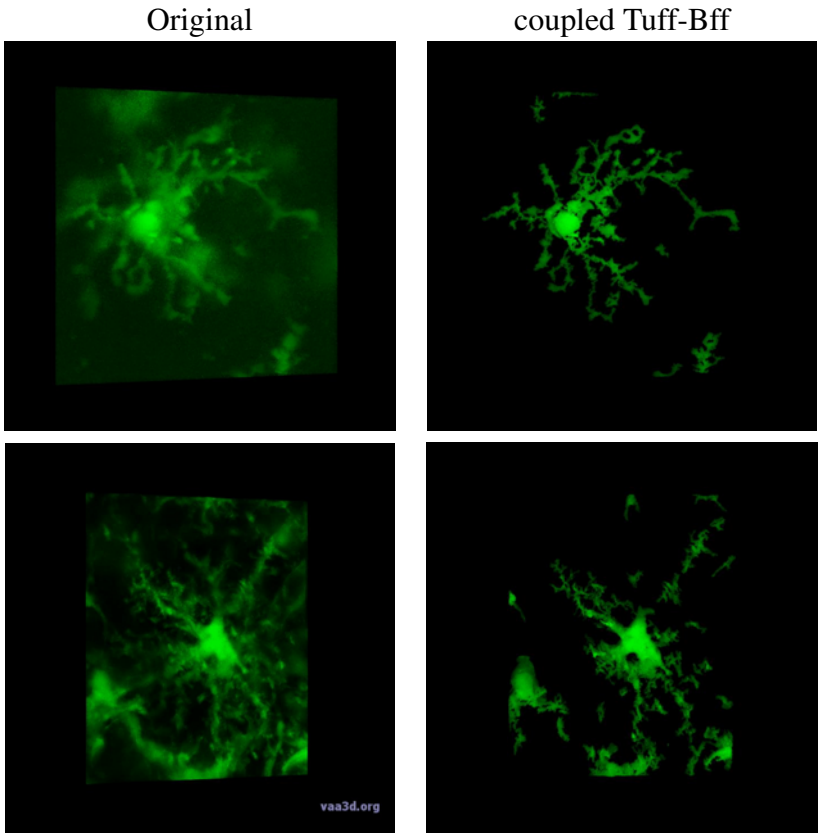

Figure 2.9: Segmentation results of microglia from healthy mouse (top row) and infected mouse (bottom row)

CHAPTER 3

TIME SERIES MOTILITY RECONSTRUCTION: ACHIEVING A CONSISTENT ANALYSIS

Accurately tracing the thin, tubular microglia processes would benefit the assessment of microglia topology and facilitate acquiring motility measurements and bioinformatics. In this chapter, we present two methods to accurately trace 3D images of microglia over consecutive time frames. First, we give a brief background on skeletonization. Then, we present the first method, *Hieroglyph*, which generates microglia skeletons over time by hierarchically matching graph to glia of subsequent time frames. We will discuss and analyze the experimental results. Next, we present our second tracing method based on Vector Field Convolution (VFC). We will give a brief background on active contour models, gradient vector fields, vector field convolution and centerline tracing. We will present our second method, *C3VFC*, which uses **v**ector **f**ield **c**onvolution and **c**oncentric **c**ircles to find the **c**ritical points that are used to trace 3D images of microglia over consecutive time frames. We will discuss the experimental results and performance evaluation of C3VFC.

The main goal of this project is to analyze temporal image data, or more specifically the movement of glia processes in different settings to understand the morphological differences in those settings. In the previous chapter, the segmentation framework is non-continuous, meaning, each 3D image in the time stack is individually segmented. The problem with non-continuous segmentation is the reconstructions may not be consistent with subsequent reconstructions within the time stack. *Consistency in this context means the reconstruction results and accuracy are agreeable over time.*

Skeletons are compact representations of an object in an image that are single pixel or voxel thick and represent the overall topology of the structure. Figure 3.1 illustrates segmentation reconstructions are skeletonized using medial axis thinning over consecutive

time frames. The skeletonizations illustrate that a slightly inconsistent segmentation over time can impact the branch information. In the top row, the original images show that microglia processes steadily extend and retract over time. However, the skeletons of the segmentation show that the processes abruptly appear and disappear through out time frames, which is not an accurate depiction of microglia movement. In Chapter 2, we discussed the challenges and difficulties of acquiring a segmentation reconstruction, due to microscopy imaging and intensity inhomogeneity. Yet, it is apparent from the figure that inconsistent reconstructions could result in an inaccurate analysis of temporal data. For example, correspondence between branches would be necessary to find the change in length or the velocity of a branch path over time. However, erroneous branch correspondence between time frames would lead to incorrect length changes and velocity measures of a branch.

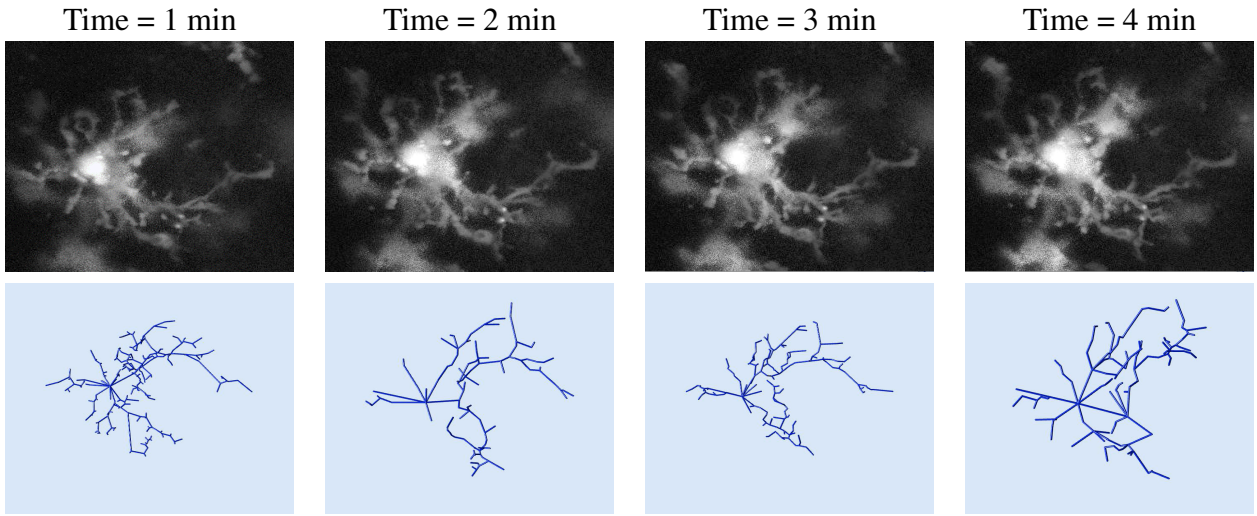

Figure 3.1: Consistent skeleton reconstructions over time is essential for morphological analysis.

3.1 Background on Tracing

Manual reconstruction and tracing is still accepted to be the gold standard. However, manually reconstructing 3D images is laborious and becomes infeasible with high-throughput imaging. As depicted in Figure 3.1, it is difficult to acquire consistent segmentations over

time. Automatic segmentation relies on the image information, however, microglia processes are thin and have intensity inhomogeneity, which attribute to inconsistent segmentations. Tracing microglia gives visually clear topological information, particularly about structural changes over time. Skeletonization is a popular method for tracing tubular biological structures like neurons and microglia. A skeleton is a single-pixel-wide tracing along the centerline of an object. A skeleton should be a topological representation of the object, meaning it should ideally follow the geometric properties of the object where components correspond to parts of the object [57]. There is disagreement on this definition of a skeleton due to the challenging process of automatically acquiring a skeleton and the requirements of various applications. In 1967, Harry Blum introduced object thinning, referred to as the medial axis transform, to present a shape descriptor that would describe biological images. Since then, thinning algorithms have been useful in the biological imaging field, including applications related to cell shape analysis [58], vessel skeletonization [59, 60], character analysis [61], fingerprint recognition, tracking and characterization of object morphology.

Blum's medial axis was found using a grassfire transform where the object is though of as dry grass, fire starts at the boundary of the objects, and the grassfire propagates towards the medial axis where it meets and forms the skeleton [62]. This has been generalized and adopted into the medial axis transform (MAT) which involves iteratively eroding the boundary of the object until only a one-voxel-thick limb remains on the "medial axis" [62]. Alternatively, the medial axis can be attained using a distance transform. The distance transform map is obtained by labeling the pixels or voxels of a binary image with their distance to the nearest background. The values on this "distance map" increases closer to the center of the image. There are various methods to acquire the skeleton from the maxima of the distance map.

Different skeletonization approaches have been generated including the minimal spanning tree. There is still a monumental amount of research to attain a medial axis that is robust and stable. The difficulty in achieving an accurate skeleton still remains, as the existing

methods are dependent on the object shape or the image intensity variations. Non-smooth and irregular structure can lead to spurious edges, false branches, discontinuities, loops and other anatomical or structural inaccuracies in the skeleton reconstruction. Such methods typically require a prior segmentation, or binarized image, of the object of interest, which makes the resulting skeleton largely dependent on the segmentation accuracy. A slight shift in the object boundary would affect the placement of the medial axis. The inaccuracies of the prior information can lead to inconsistent and erroneous skeletonization. Consistency is necessary in analyzing temporal image data to attain accurate analysis. We aim to create a joint framework in which reconstruction results are used to create reconstructions of other images within the same time stack.

3.2 Hieroglyph: Matching Glia and Graph

Our method *Hieroglyph* generates consistent glia over time by hierarchically matching graph to glia of a subsequent time frame, hence its name. *Hieroglyph* produces a consistent temporal digital reconstruction of a glia skeleton by using prior information from previous 3D acquisition. The skeleton from a previous acquisition is evolved by representing the cell as a graph where the glia process lengths are stored as edge information and each bifurcation is stored as a node. In Section 3.2.1, we describe the use of the graph representation of the glia to achieve a skeleton tracing using a shortest path algorithm. In Section 3.2.2, *Hieroglyph* evolves the previous skeleton to match the image in the next time frame. Each generated skeleton is employed to create another consistent 3D skeleton for the following glia image in the time series.

3.2.1 3D skeleton: shortest path in a graph

Let us consider a set of 3D time series images where the segmentation of the image at time t=1 is represented as an adjacency matrix of an undirected, weighted, rooted tree graph, *Adj(G)*. The graph consists of vertices and edges, *G=(V,E)*, where the vertices are initialized

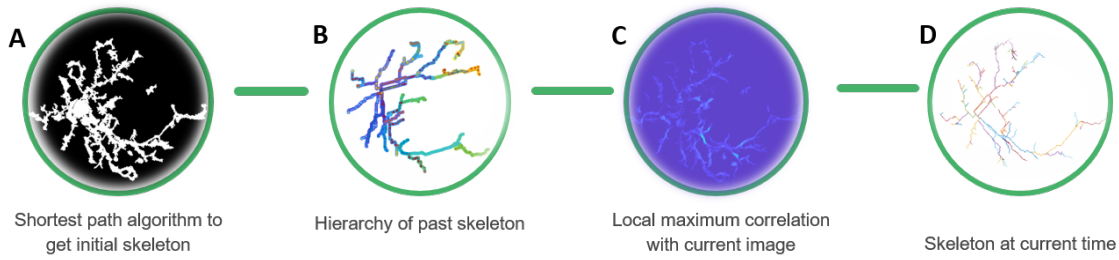

Figure 3.2: Overall methodology. A) The shortest path is take from the end node to the soma to get the first skeleton. B-C) a skeleton is morphed to another in an hierarchical manner D) the resulting skeleton. (B-C) is repeated for the remaining images in the time series.

at every foreground pixel in the segmented image and size of V equals the number of foreground voxel in the segmented image. The edges are weighted by the spatial Euclidean distance between the voxels, $e = 1, \sqrt{2}, or \sqrt{3}$ [63, 64]. The adjacency matrix is filled with the weights of the edges between all the foreground voxels. The size of *Adj(G)* is $N \times N$ where N is the number foreground pixels, or the number of vertices.

From a biological standpoint, we know that our reconstructed graph is a simple graph which should not contain any loops or discontinuities from the processes to the soma of the glia. Thus, to implement our tracing of the cell, we use Dijkstra's algorithm [65] to find the shortest path between the terminal nodes of the processes to the soma of the glia. The terminal nodes are extracted from the segmentation of the 3D glia, and the soma vertex is the center of mass of the 3D soma segment. The algorithm starts at terminal node and finds the shortest route within the given adjacency matrix of the graph to the soma, or root node. The route of the voxels between the soma and the terminal nodes result in a 3D skeleton tracing of the glia. *The benefit of the graph representation is the rich information provided that includes the hierarchy of the processes, the bifurcation points, and the endpoints.* These properties are exploited in the creation a consistent skeleton for the subsequent glia image in a time series.

3.2.2 Consistent 3D skeletons from temporal information

Acquiring glial skeletons solely from segmentation can result in inconsistencies between acquisitions in time and is computationally burdensome. A single glia cell over time extends

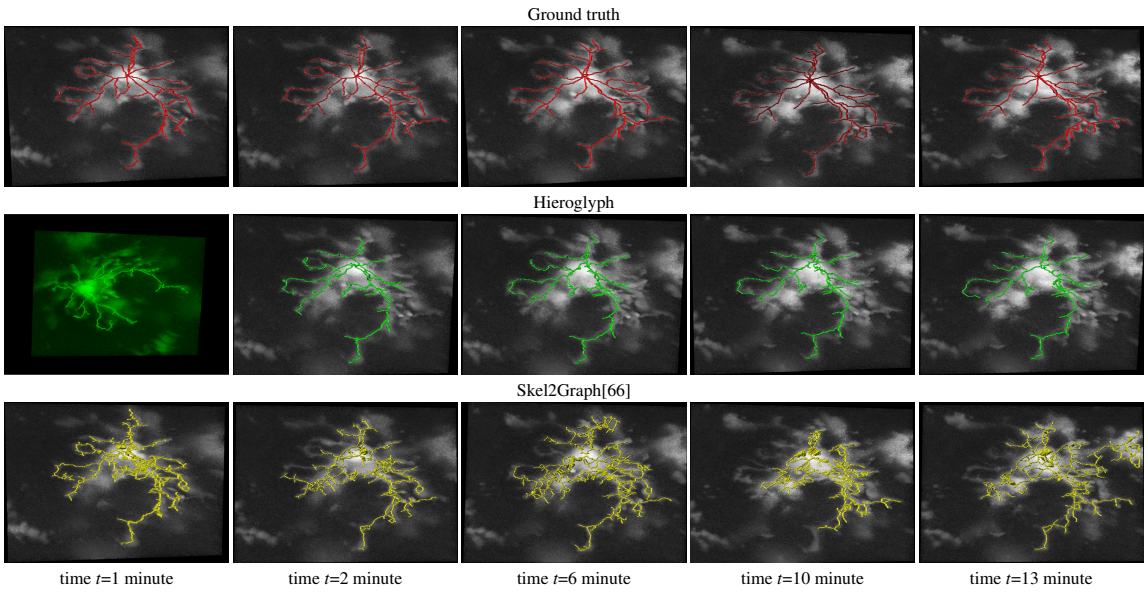

Figure 3.3: Segmentation results of 3D microglia images.

and retracts the processes while keeping the same number of branches that emerge from the soma. Thus the morphology of a glial cell between subsequent acquisitions is consistent. We propose a method that uses prior temporal information combined with intensity information from the current image. *Hieroglyph* seeks to drive the skeleton from a previous time frame to the vessel-like information in the original image of the current time stack.

The latter information is gathered by using the Hessian-based vessel enhancement technique to distinguish tubular structures in an image. This technique utilizes a multiscale function according to three direction of the orthonormal eigenvectors, $\mathbf{e}_i(\mathbf{x})$, where $\mathbf{x}$ is the pixel position within the image domain [53, 67]. These directional eigenvectors are attained by computing the Hessian matrix of a Gaussian smoothed 3D image and then ordering the eigenvectors by the increasing magnitudes of the eigenvalues $|\lambda_1| \leq |\lambda_2| \leq |\lambda_3| >> 0$. A vessel-enhanced image is obtained with a low $|\lambda_1|$ value and high $|\lambda_2|$ and $|\lambda_3|$ magnitudes. We call the vessel enhanced image I_v.

The initial skeleton from the previous time frame, S_{t-1} is broken into hierarchies, where the root node is equal to 0 and the hierarchy increases toward the terminal branches. Every bifurcation of a process separates the process into another hierarchy H, where $H = h_1, h_2, ...h_i$ is a set of hierarchies, length i. Every segment belongs to a cluster h_i

within the set. The algorithm morphs the skeleton, one segment at a time, starting from the lowest hierarchy until it achieves the maximum response with the vessel enhanced image. This is repeated for all segments of the skeleton in H. The final skeleton at time *t* is given by

$$S_t = \max \sum_{h=1}^{i} S_{t=1}(h^*) I_v \tag{3.1}$$

$$I_v = \begin{cases} x & x > 0, \\ -x_{avg} & x \leq 0. \end{cases} \tag{3.2}$$

where h^* is the morphed segment from the previous skeleton and x is the voxel value in I_v. The morphing of the segments are changes in the 26 cardinal directions. The morphed segments are bounded by the following conditions: 1) The first hierarchy must start at the root node. 2) Segments may not overlap with each other (no loops). 3) The bifurcation points are regularized so they do not drastically move.

The zero intensity values in I_v are set to the negative value of the average pixel intensity to penalize morphing beyond vessels in the Hessian map. Once a new segment is created, the tree is rerouted resulting in an updated graph representation of the skeleton so that the routes and bifurcation nodes are updated.

3.2.3 Experimental Results and Analysis

The dataset consists of 3D images of microglia imaged from healthy mice brains using multiphoton microscopy, as explained in Section 1.3.

In our experiments, the segmentation at time *t* = 1 was attained using the coupled tubularity flow field and blob flow field (Tuff-Bff) algorithm [68].

3.2.3 Performance Evaluation

We use a dataset consisting of 3D images of microglia over a time of 13 minutes. We compare our reconstruction of temporal skeleton results with an automatic skeleton reconstruction

method called Skel2Graph3D, which requires a 3D segmentation of the original image at each time and was used to reconstruct osteocyte cells [66]. This was done as a comparison, because osteocytes are similar in morphology to microglia. Their 3D skeletonization function is based on a medial axis thinning algorithm [69, 70], but the Skel2Graph3D algorithm iteratively prunes the skeleton and converts it into graph representation. The ground truth was attained using the Simple Neurite Tracer in ImageJ, which is a semi-automatic tracing software [71]. We compare the accuracy of the *Hieroglyph* results and the state-of-the-art comparisons with the ground truth. We note that even the ground truth may have user error due to background noise and intensity inhomogeneity throughout the object of interest.

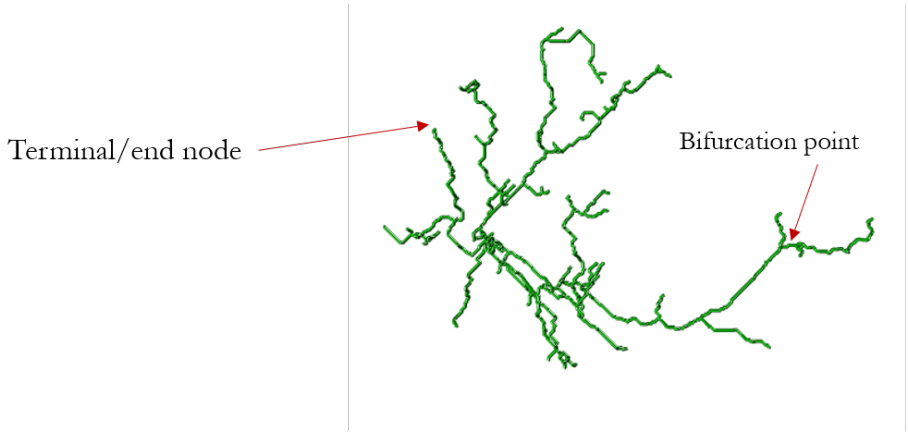

Figure 3.4: The endpoints and bifurcation points can easily be determined from the hieroglyph.

From Figure 3.4.2.2, *Hieroglyph* has a consistent structure over time. The algorithm maintains consistency by its working principle. But the spatiotemporal localization of the consistent skeletons are obtained within a margin of error. Our temporal results are based on the result of the prior image but we can see that the skeleton over time changes as the cell changes. We use a hierarchical weighting method to compare the accuracy scores. The branches in each hierarchy are counted and the true and false count is attained by comparing with the ground truth and the accuracy $\frac{TP}{TP+FP+FN}$ is attained for each hierarchy. The final accuracy is found by giving a higher weight to the hierarchies closest to the soma, or the primary branches. The weight is established with the factorial of the maximum number

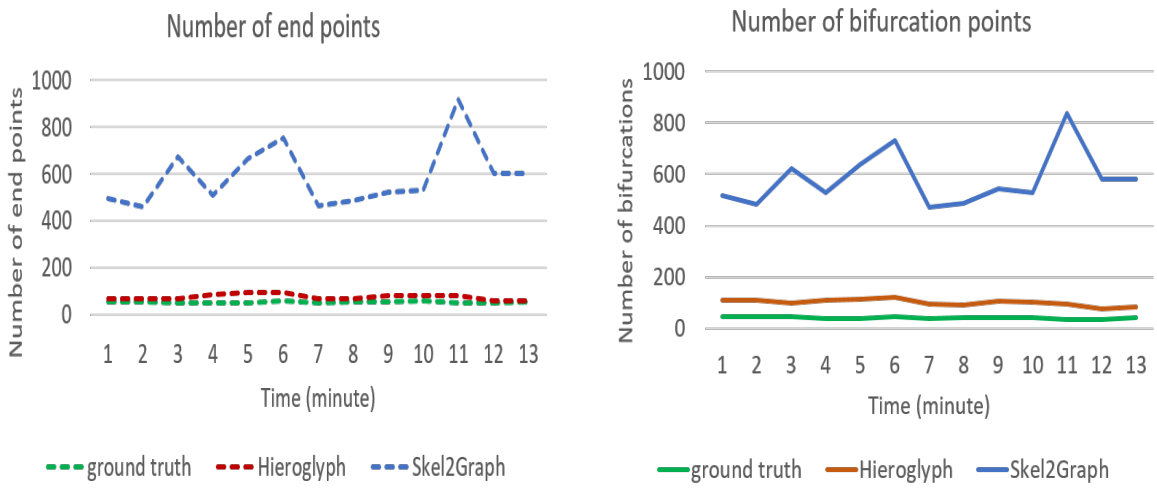

Figure 3.5: Performance evaluation using the number of endpoints (left) and bifurcation points (right) of the results from the ground truth, Hieroglyph, and Skel2Graph.

of hierarchies times the accuracy at each hierarchy given by $A_{total} = H^{gt}_{\max}! \sum_{n=0}^{i} A_{Hn}$ where H_{gt} is the number of hierarchies in the ground truth and i is the total number of hierarchies in the test image. This final accuracy for *Hieroglyph* for the first time stack is 55% for *Hieroglyph*, and 34% for Skel2Graph. Since the accuracy of the skeleton over time is dependent on the accuracy of the first skeleton, we consider additional measurements for comparison.

We measure the number of bifurcation points and number of terminal nodes as well as the distance between the results and the ground truth, as shown in Figure 3.6. The endpoints and bifurcation points on a hieroglyph can be depicted in Figure 3.4. The number of bifurcation points and terminal points in *Hieroglyph* results remain consistent with the number of bifurcation points in the skeletons from the ground truth, which is further shown in the graphs in Figure 3.5. The Skel2Graph has a significantly greater number of bifurcation points and endpoints due to the loops. The distance between the bifurcation points and endpoints of the ground truth's and that of *Hieroglyph* and Skel2Graph are calculated. The measurements show how structurally similar the resulting skeletons are compared to the ground truth skeleton. Figure 3.7 shows that a 3D skeleton rotated to make processes

Time:		1 min.	3 min.	8 min.	11 min.	13 min.
No. of bifurcations	Ground truth	46	44	41	35	41
	Hieroglyph	62	55	51	60	42
	Skel2Graph	408	522	393	744	498
No. of end nodes	Ground truth	54	48	52	49	55
	Hieroglyph	65	69	65	79	58
	Skel2Graph	495	672	487	920	601
Bifurcation distance to ground truth (voxels)	Hieroglyph	8.87	9.259	13.3	14.54	10.29
	Skel2Graph	12.4	14.9	14.6	16.6	20.99
Endpoint distance to ground truth (voxels)	Hieroglyph	14.62	10.9	17.05	16.94	14.05
	Skel2Graph	14.06	12.2	17.8	19.46	17.89

Figure 3.6: Structural measurements compared to the ground truth.

extending in the z-direction more visible. Some processes described may not be visible or be accurately distinguished in a 2D image. This motivates a 3D skeleton for morphological and motility analysis.

3.2.4 Remarks

In this section, we proposed an automatic temporal 3D skeletonization method for glia images. We are able to use the *a priori* information from preceding skeletons to derive subsequent ones. The method is hierarchical since the skeletonization and graph matching are performed in segments starting at the soma and extending to the endpoints of the processes. *Hieroglyph* attained consistent skeleton structures over time. Unlike other skeletonization or tracing methods that lose volumetric information of the structure, the graph representation is not only *minimalistic and compact*, *Hieroglyph* retains information about the diameter of the original image at every point while understanding the spatial relationship between the soma, bifurcation points, and terminal points of the processes.

While our method performed better than the state of the art, the algorithm could be

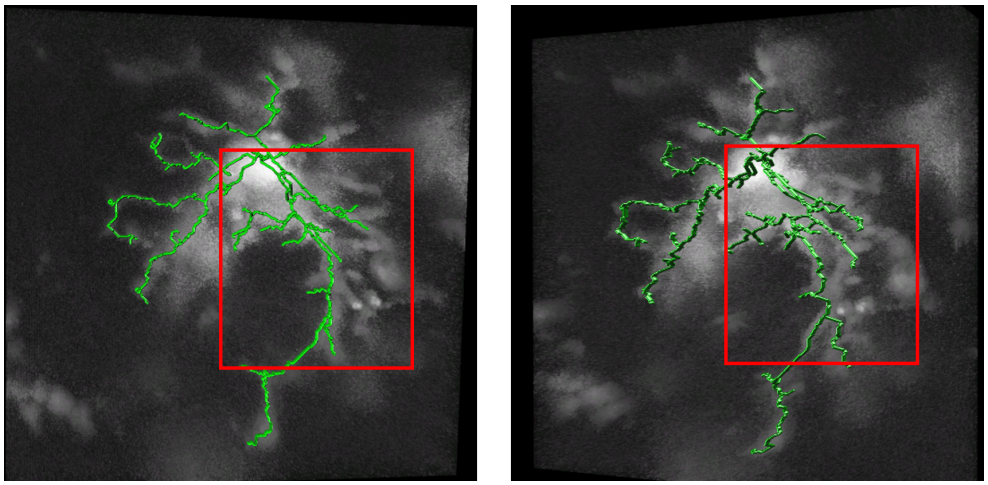

Figure 3.7: A skeletonization of a glial cell in one orientation (left) and a 3D rotation of the same (right). The rotated view reveal branches not shown in the original view motivating 3D analysis.

further improved to increase the accuracy of the reconstructed skeleton. For the current implementation of *Hieroglyph*, the accuracy of all the skeletons in the time series is dependent on the skeleton reconstruction at the first time. To reiterate, the initial skeleton is reconstructed by finding the shortest path from the end nodes to the soma (center of mass of the soma) of the segmented image. Thus, the accuracy of the skeleton is dependent on the number of correct terminal nodes found.

One of the measurements we want to analyze associated with glia are the ramification of processes over time. For most cases, this means measuring the length of a processes. However, this could also mean there are appearances and disappearances of smaller branches. Past works that have analyzed glia motility do not account for these addition and deletion of branches over time. It is a difficult problem consider in automatic algorithms. In future improvements, we would like to account for the branches that may appear or disappear in subsequent frames. The temporal images may have a drifting of the objects of interest because the mice may be moving during the imaging. A solution to account for this in our tracking algorithm could be finding and assigning the bifurcation points in subsequent frames. Accounting for the addition and deletion of processes could also improve the accuracy in case some branches may not have been captured in previous frames. Thus, the

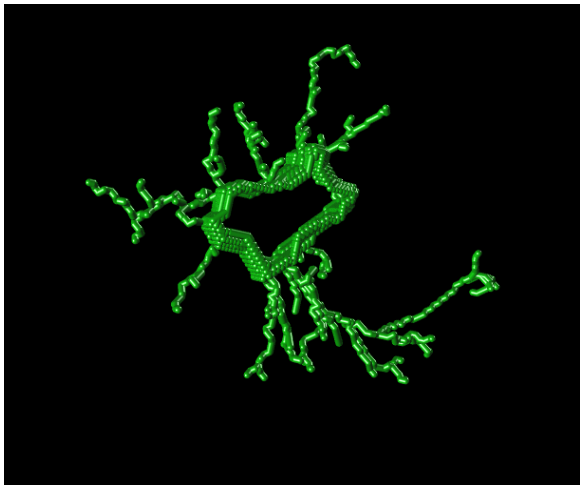

Figure 3.8: Graph representation with soma.

accuracy of the skeleton over time would not be completely dependent on prior frames.

In *Hieroglyph*, the soma is represented by the center of mass which is just one point. This single-point representation could change the path of the processes and thus the analysis of the processes. Instead of representing the soma as just one point, the algorithm should account for the whole soma. This means that in the first part of the algorithm, we should find the shortest path from the end point to the whole soma, or the nearest point of the soma, as shown in Figure 3.8. This graph is no longer a tree since the soma in itself is a loop. If we were to need an acyclic graph, the graph could be translated such that the soma is represented by a point. However, initially keeping the soma shape may produce more accurate skeletons.

3.3 Improving Centerline Tracing with Vector Field Convolution

In this section we create an algorithm that simplifies the tracing algorithm using Vector Field Convolution. Our method does not require preprocessing, greatly reduces the computational time of previous tracing methods, and improves on accuracy of the centerline tracing. This method provides consistent morphological reconstructions that is imperative to analysis, as proven in Section 4.

3.3.1 From parametric active contours to vector field convolution

In Section 2, we designed a method to look for the image boundary using an active contour method. In that section we discussed how the active contour is first initialized in the image of interest. Next, the contour is iteratively evolved until it reaches the desired boundary where it stops, or converges. Often times, the active contour evolution follows the gradient magnitude of the image, however, a gradient external force can be limited by its capture range. The gradient magnitude of an image's homogeneous regions are zero or close to zero which may cause the active contour to get stuck before reaching the desired boundaries. This limitation makes some models to reliant on the initialization of the contour, which in turn is not very robust. The gradient external force also caused issues in cases where the edges were concave or the initial contour was too far from the minimum.

Geometric active contours, mentioned in Chapter 2, are an implicit active contour model. Parametric active contours are, rather, explicitly defined where the contour C is represented as

$$C = \{x \in \Omega : x = (x_1(s), x_2(s), 0 \leq s \leq 1\} \tag{3.3}$$

where $x_1(s)$ and $x_2(s)$ are parameterized point locations along the contour C with landmark s. Parametric active contours were first defined by Osher and Sethian [72]. The contour is discretely parametrized with a finite number of pixels, or snaxels, as in equation 3.3, and the evolution is explicitly computed with the forces at each of the snaxel positions.

Some limitations include problems with re-initialization, and issues with converging at boundary concavities. A new external force, called gradient vector flow (GVF), was developed by Xu *et al.* [73] to address the issue of capturing an adequate capture range. The GVF is computed from the diffusion of the gradient vectors $(u(x, y), v(x, y), w(x, y))$ of either the gray level image or the edge map of an image. The GVF is computed by

minimizing the energy functional:

$$E_{GVF} = \frac{1}{2}\int\int \mu(u_x^2 + u_y^2 + v_x^2 + v_y^2) + (f_x^2 + f_y^2)((u - f_x)^2 + (y - f_y)^2)dxdy \quad (3.4)$$

where μ is the smoothness parameter of the GVF force field and (f_x, f_y) is the edge force. GVF diffused external force gave a better capture range that was further from the object so that initialization was (less forgiving). Vector field convolution (VFC) also computed the diffused external force using convolution, a compututionally less expensive method than finding the GVF via diffusion. VFC fields are more robust to noise and initialization than the classical gradient field convolution[48]. It was used to reconstruct a skeleton for neuron images in [74] by acquiring a VFC medialness map to find a binary image to thin and then reconnect with a graph minimum spanning tree. However, these methods rely on finding the correct scale to accurately reconstruct the image but result in disjoint segments and noisy reconstructions. The authors used Tree2Tree and Tree2Tree2 attempted to reconnect disjoint segments using a graph connectivity algorithm that relied on orientation and distance[75, 63]. However, attempting to reconnect disjoint segments in glia images with orientation and distance result in incorrect connections due to the complexity of branches within one cell and between one another. Our method proposes to use VFC field to evolve seed points towards the centerline.

3.3.2 Background on Vector Field Convolution

Vector field convolution (VFC) was proposed as an external force field for an active contour method used in image segmentation. The basic idea was to compute vectors that pointed at image edges and then to diffuse such forces across the image via tensor convolution. The resultant VFC fields are robust to noise and to initialization of an active contour [48]. The convolution-based approach was also used to reconstruct a skeleton for neuron images in [74] by acquiring a VFC medialness map, an enhanced medial-axis image, which they

used to create a graph minimum spanning tree. However, these methods rely on finding the correct scale to accurately reconstruct the image, but result in disjointed segments due to intensity inhomogeneity and noisy images. The authors attempted to reconnect the disjointed segments using a graph-connectivity algorithm that was based on the orientation and distance of the segments from one another [75, 63]. Attempting to reconnect disjointed segments in glia images based on orientation and distance result in incorrect connections due to the complexity of branches within one cell and between other intra-cell branches.

Our method, C3VFC, utilizes VFC in an open curve tracing methodology to find the critical points and the centerline, or skeleton, of multiple objects within 2D and 3D videos. This technique, based on VFC, is an enabling image analysis technology that paves the way for reliable microglia reconstruction.

In [48], the open curve is a parametric active contour model that is deformed toward edges in the image, controlled by the external and internal energy. The external force guides the active contour towards the edges using image features. The internal force is guided by the qualities of the contour, such as smoothness or tautness. The contour is represented as a set of contour points $\mathbf{v}(s) = [x(s), y(s), z(s)]$ and the initial points are parameterized between $s \in [0, 1]$. The initialized contour is evolved by minimizing an energy functional:

$$E = \int_0^1 [\frac{1}{2}(\alpha|\mathbf{v}'(s)|^2 + \beta|\mathbf{v}"(s)|^2) + E_{ext}(\mathbf{v}(s)]ds \tag{3.5}$$

where α and β are the parameters for controlling smoothness and bending of the contour, respectively. In [48], the authors defined the external energy, E_{ext}, with the Vector Field Convolution force, $\mathbf{f}_{vfc}(\mathbf{v})$.

An active contour model for open splines needs to be constrained so that the points along the contour do not drag into itself and vanish. For every iteration, the curve is updated where the set of contour points may shrink or grow. For a vector field that points towards the medial axis of an object, the intensity inhomogeneity within the object may cause parts

of the medial axis to have a greater pull on the vector field. However, constraining the end points of a contour for a non-continuous structure, such as a microglia, typically involves splitting an object into multiple parameterized contours, or branches. In [40], the authors constrained the open curve by evolving the contour one point, or seed, at a time, controlling the elasticity and connection of all seed points to each other, which, if used in larger data sets, could be computationally expensive. Other open curve active contour methods improved on this work by automatically initializing fewer, more accurate, seed points to evolve the seeds toward each other following the gradient vector field [76, 77, 78]. These methods largely rely on finding seeds that are already initialized on the centerline.

3.4 C3VFC: Tracing 3D Images of Microglia Over Time

C3VFC is our automated tracing system that computes the skeleton of objects in a 3D image over sequential time frames, which facilitates accurate biological analysis and quantification via extraction of bioinformatics. The method is described in Figure 3.9 and in Algorithm 1. The number of objects in the image are determined by automatically detecting the soma, or the cell body, and its corresponding critical points, so that each object can be individually traced in parallel. Critical points are detected for each object by evolving seed points, or the initialized points, that are constrained by *concentric circles* around each soma. The final temporal skeletons are extracted via a fast marching method from the critical points and a centerline map. The temporal reconstructions can be used for accurate biological analysis. In this paper, we compare our reconstruction results from C3VFC and from state-of-the-art methods with those derived from the baseline standard manual tracing.

3.4.1 Overall Methodology

A 3D vector field is computed using vector field convolution [48] on the original image, $I(x, y, z) \in \mathbb{R}^3$, to find the centerline that lies on maximum intensity of an object, which is also the centerline of the object. A vector field kernel, $\mathbf{k}(x, y, z)$, is convolved with $I(x, y, z)$

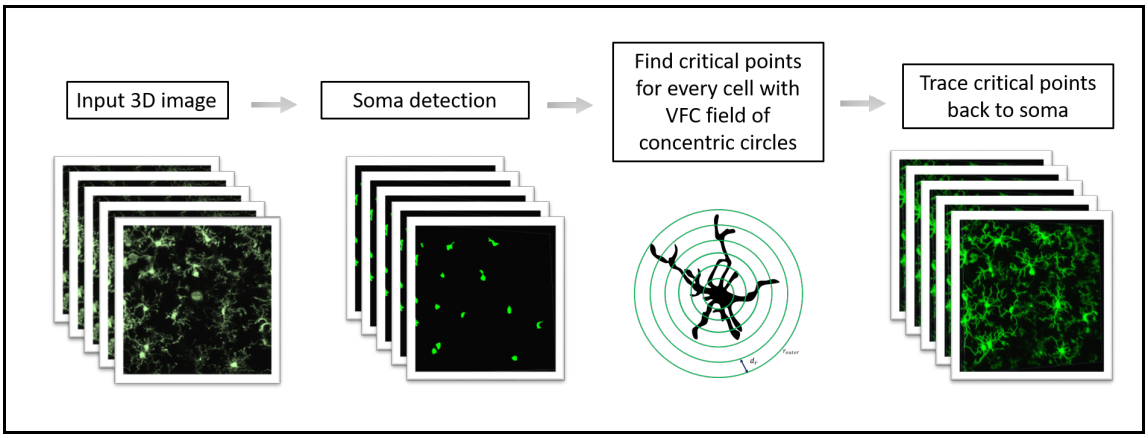

Figure 3.9: C3VFC methodology.

so that the vector field points towards the centerline. The vector field is defined as:

$$\mathbf{f}_{vfc}(x, y, z) = I(x, y, z) \circledast \mathbf{k}(x, y, z) \tag{3.6}$$

where $\circledast$ is defined as linear convolution. The vector kernel is defined as:

$$\mathbf{k}(x, y, z) = m(x, y, z)\mathbf{n}(x, y, z) \tag{3.7}$$

where $m(x, y, z)$ is the magnitude of the vector kernel and $\mathbf{n}(x, y, z)$ is the unit vector pointing towards the kernel origin at (0,0,0):

$$\mathbf{n}(x, y, z) = [-x/r, -y/r, -z/r] \tag{3.8}$$

that is normalized by the radius $r = \sqrt{x^2 + y^2 + z^2}$ which is the distance from the origin. The origin of the kernel, (0,0,0), is considered the location of the features of interest (FOI), so a particle that is placed in that field is able to move towards the FOI, which in this case is the centerline. The magnitude of the vector kernel is:

$$\mathbf{m}(x, y, z) = (r + \epsilon)^{-\gamma} \tag{3.9}$$

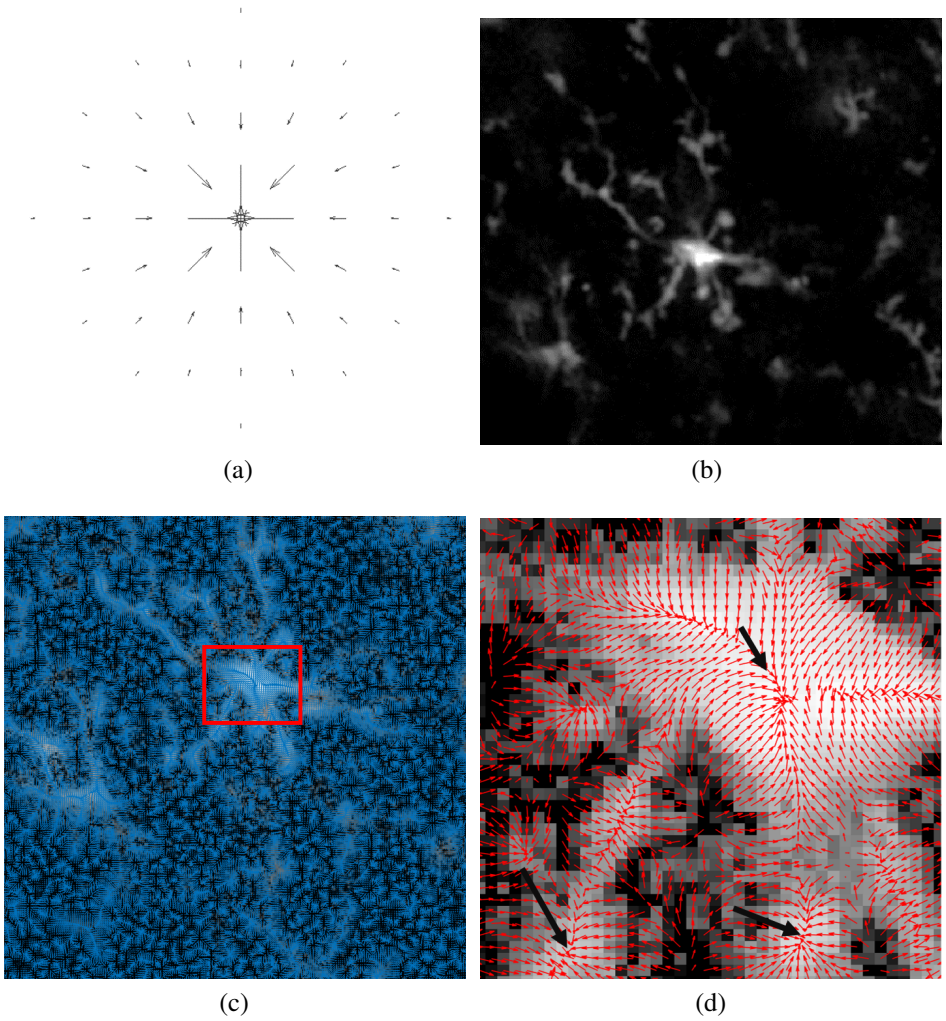

Figure 3.10: The VFC field of the intensity image **a)** The kernel is convolved with **b)** the original image (slice 8 of 16 in the z-stack is shown) to produce **c)** VFC field **d)** zoomed in of the red box in **(c)**. The arrows point to areas of higher intensity that pull the vectors on the centerline of the object.

where γ is a parameter that controls the influence of the FOI, and should be changed according to the signal-to-noise ratio. ϵ is a small positive constant that avoids dividing by zero. Thus, the further away the particles are from the origin, the smaller the influence of the FOI, and the magnitude of the vector field kernel is a decreasing function of distance from the origin. Figure 3.10a shows a vector kernel where the magnitude of the vectors decreases as the they are farther from the origin.

The VFC external force $\mathbf{f}_{vfc}(x, y, z)$ is calculated by finding the convolution between the

vector field kernel $\mathbf{k}(x, y, z)$ and the intensity image $I(x, y, z)$. For a 3D image, the VFC force field would be comprised by a three directional vector field in which the vectors point towards the centerline of a 3D object.

Figure 3.10 depicts the VFC field on a microglia image. A 3D image of microglia is convolved with the vector kernel in equation 3.7 to produce a VFC field that points to the centerline of the objects. Although the figure depicts a slice from the z-stack, the 3D vector field points to the center line in x-y-z direction. The vector's magnitude and direction relies on the intensity of the image and the parameters of the kernel. In a real image, the noise pulls the vectors in the background but the large capture range of the kernel pull the vectors towards the higher intensity of the foreground object, or the centerline.

In biological images, there may be varying intensity throughout the object, where some intensities may be stronger in thicker parts of the object. Figure 3.10d shows that the vectors along the centerline point towards higher intensities within the object. Thus, there are non-zero vectors on the centerline that would move free particles towards a converging point. However, in open curve tracing we would ideally want the particles to stop at the centerline. Our workflow solves these challenges by detecting and labeling the cells, using the VFC field to find critical points in the cells, and tracing critical points back to the soma.

3.4.1 Initialization

The goal of C3VFC is to trace glia in single- and multi-cellular 3D images, I, over consecutive time frames. Biological images acquired through microscopy imaging have low signal-to-noise ratio (SNR) and background noise so we want to ensure that the points are evolved within the region of interest. The Hessian matrix of partial derivatives describes the local curvature of an image [79]. The visualization of the initialization is depicted in Figure 3.11. The eigenvector of the Hessian describes the concavity at points in the image. The attained eigenvectors can be sorted via by the absolute value of their eigenvalues. The most negative eigenvalue, λ_3, describes the highest curvature. The voxels at which $\lambda_3 > 0$

is set to zero. The remaining voxels are the foreground pixel in I_{fore}. This will be the initial seed points that will be evolved towards the centerline of the parts of the object via our open curve tracing method.

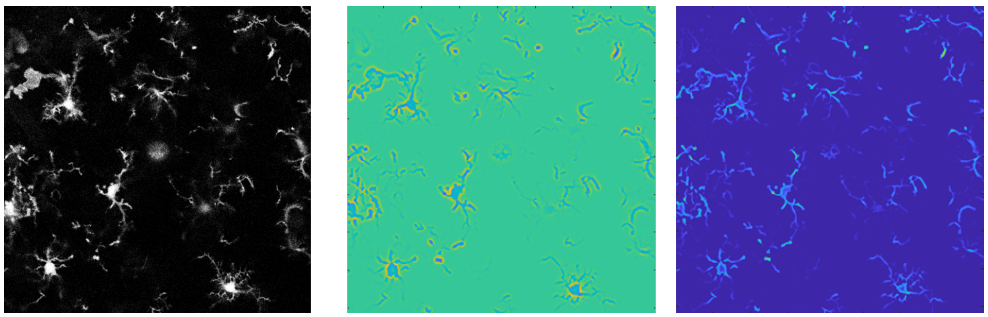

Figure 3.11: The initial seed points are determined using curvature analysis. The original image (left) is analyzed with a curvature analysis (middle) to find the foreground image (right).

3.4.1 Soma Detection and Labelling Cells Over Time

In glia cells, the processes extend and retract from the soma. The cell bodies can be utilized to determine the number of cells and its respective processes in an image. The soma can be distinguished by its overpowering intensity and volume compared to the fine processes. We automatically detect and reconstruct the soma from the input image via the blob flow field (BFF) method [68]. In this approach, eigenvectors attained from the Hessian matrix of a Gaussian-smoothed image are ordered by increasing magnitude of the eigenvalues, $|\lambda_1| \leq |\lambda_2| \leq |\lambda_3| \gg 0$ [53]. BFF enhances blob-like structures by finding structures in the image with high values of λ in the three orthonormal directions. Once the blobs are detected, the edge based active contour algorithm moves the contour towards the soma boundary.

The soma detection method finds s somas in the given input image, which is used to label detected soma over consecutive time frames. As seen in Figure 3.12, it is difficult to determine soma shape and separate touching cells in 2D images, which are z-stack projections of the 3D image. Some cell processes and soma may be overlapping or occluded in the z-stack of a 2D view. However, a tilted view of the 3D image reveals the actual number of cells in a given region. Knowing the correct number of cells and soma shape allows our

algorithm to trace the processes back to the appropriate soma. Figure 3.12c shows some processes that belong to cells where the soma is not in the field of view and only portions of a cell are captured. This inevitable issue presents a challenge for constructing the tracing methodology. It can be argued that only cells that are fully in the region of interest need to be segmented for quantification and analysis. C3VFC uses the detected soma to find and label the corresponding soma over consecutive time frames. Consequently, corresponding glia are automatically labelled over time with respect to their corresponding soma.

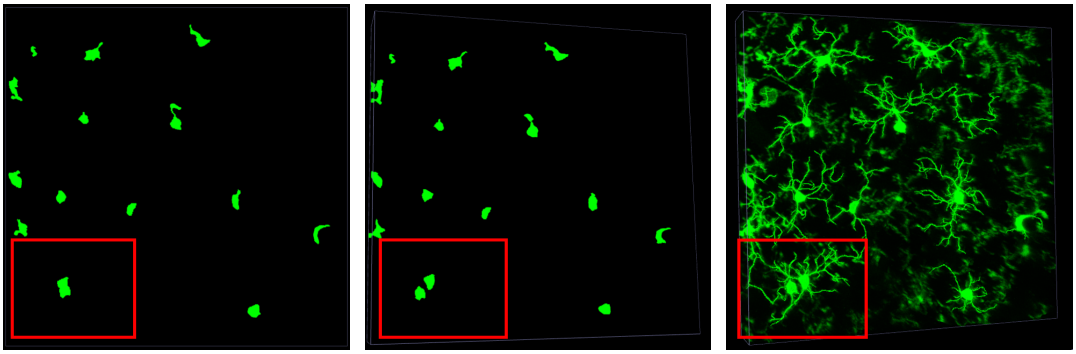

(a) (b) (c)

Figure 3.12: Soma detection **a)** 2D view, **b)** 3D view and **c)** 3D tracing of each cell. The red box in the images indicate the region of interest where soma overlap and would be difficult to distinguish in the top 2D projection of the 3D image.

3.4.1 Tracing Multiple Objects in a 3D Image

The objects in the images, or cells, are non-continuous points that are connected at the soma. These points could be parameterized in segments, as with the methods mentioned in Section 3.3.2, or represented as free particles without an internal force, as in equation 3.5. Since the seed points are non-continuous, the internal force of the active contour energy functional would not acquire the desired smoothing and bending constraints. Therefore, the energy functional would be dependent on the VFC field from Equation 3.6. The initial contour points for the image $I(x, y, z)$ is $\mathbf{v}(s) = [x_i(s), y_i(s), z_i(s)]$ which is represented by

N discrete points $\mathbf{v}_i, i \in 0, 1, 2, , , N-1$. The update procedure is iterative

$$\mathbf{V}^{t+1} = \mathbf{V}^t + \tau\mathbf{F} \tag{3.10}$$

where τ is the step size,

$$\mathbf{V}^t = [\mathbf{v}_0^t, \mathbf{v}_1^t, \mathbf{v}_2^t, ...\mathbf{v}_{N-1}^t]^T \tag{3.11}$$

and

$$\mathbf{F}^T = [\mathbf{f}_{vfc}(\mathbf{v}_0^t), \mathbf{f}_{vfc}(\mathbf{v}_1^t), \mathbf{f}_{vfc}(\mathbf{v}_2^t), ...\mathbf{f}_{vfc}(\mathbf{v}_{N-1}^t)]^T. \tag{3.12}$$

The VFC field for the image contains vectors on the centerline that point to higher intensity values within the object of interest. Vectors along the centerline may cause points to vanish into each other instead of providing a continuous tracing. To resolve these open curve tracing issues, our method finds critical points throughout the object.

3.4.1 Concentric Circles, VFC, Critical Point Detection

The cells in the image are detected via soma detection and corresponding cells are labeled over consecutive time frames. Thus, all the processes can be traced back to its corresponding soma. As mentioned in Section 3.3.2, critical points are typically determined through an eigenvalue analysis of the image vector field and represent the structural changes along the object of interest. In C3VFC, the critical points are determined by using an active contour evolution using the vector field of concentric spheres around each glia. The concentric circles are placed around the soma of every detected cell, shown in Figure 3.13a. The concentric circles are

$$S(x, y, z) = (x-a)^2 + (y-b)^2 + (z-c)^2 - (r_{soma} + (d_{CC} \cdot i))^2 \tag{3.13}$$

where the coordinates (a, b, c) represents the soma, r_{soma} is the radius of the soma, and d_{CC} is the distance between the concentric circles, and $i \in [1, M]$ where M is the maximum

number of concentric circles. The distance between concentric circles, d_{CC}, is a user-input parameter. The maximum number of concentric circles, M, is determined by the farthest initialized distance from the soma divided by d_{CC}. The vector kernel, from equation 3.7, is convolved with the intersection of the concentric circles and the intensity image to find the vector field:

$$\mathbf{f}_{vfc_CC}(x,y,z) = S(x,y,z)I(x,y,z) \circledast \mathbf{k}(x,y,z) \tag{3.14}$$

This force field constrains the evolution of seed points to the spheres to ensure that the critical points are constrained to the centerline on these areas, as shown in Figure 3.13c and 3.13d. equation 3.14 is a important contribution in our method that uses the VFC field to find the critical points in an object that lie on the centerline. In this case, we only want to evolve the initial points that lie on the concentric spheres around the objects. The initial contour points is extracted from the initial foreground image explained in Section 3.4.1.1: $V_{fore} = I_{fore} > 0$ that also intersect with concentric circles for a given soma, $V^s_{fore} = V_{fore} \cdot S^s(x,y,z)$. Figure 3.13 shows that the vector field will carry the seeds to the critical point on the intersection of the branches and the concentric sphere, using equation 3.10. The updated foreground vertices become the *critical point list* which is used to trace processes back to the soma of each microglia.

3.4.1 Tracing cells back to soma

The critical points described in the previous section lie on the centerline of the processes. Each point from the critical point list is traced back to the soma detected in the first step of C3VFC. The critical points and the soma could be thought of respectively as the start and end points on a path. The path that reaches the endpoint in a least amount of time within an image domain $\Omega \subset \mathbb{R}^3$ is the geodesic path. The minimal path problem can be solved with the Multi-Stencil Fast Marching algorithm [80]. The time arrival map is initialized with the result of the initial foreground, V_{fore}, updated using the VFC field from equation 3.6.

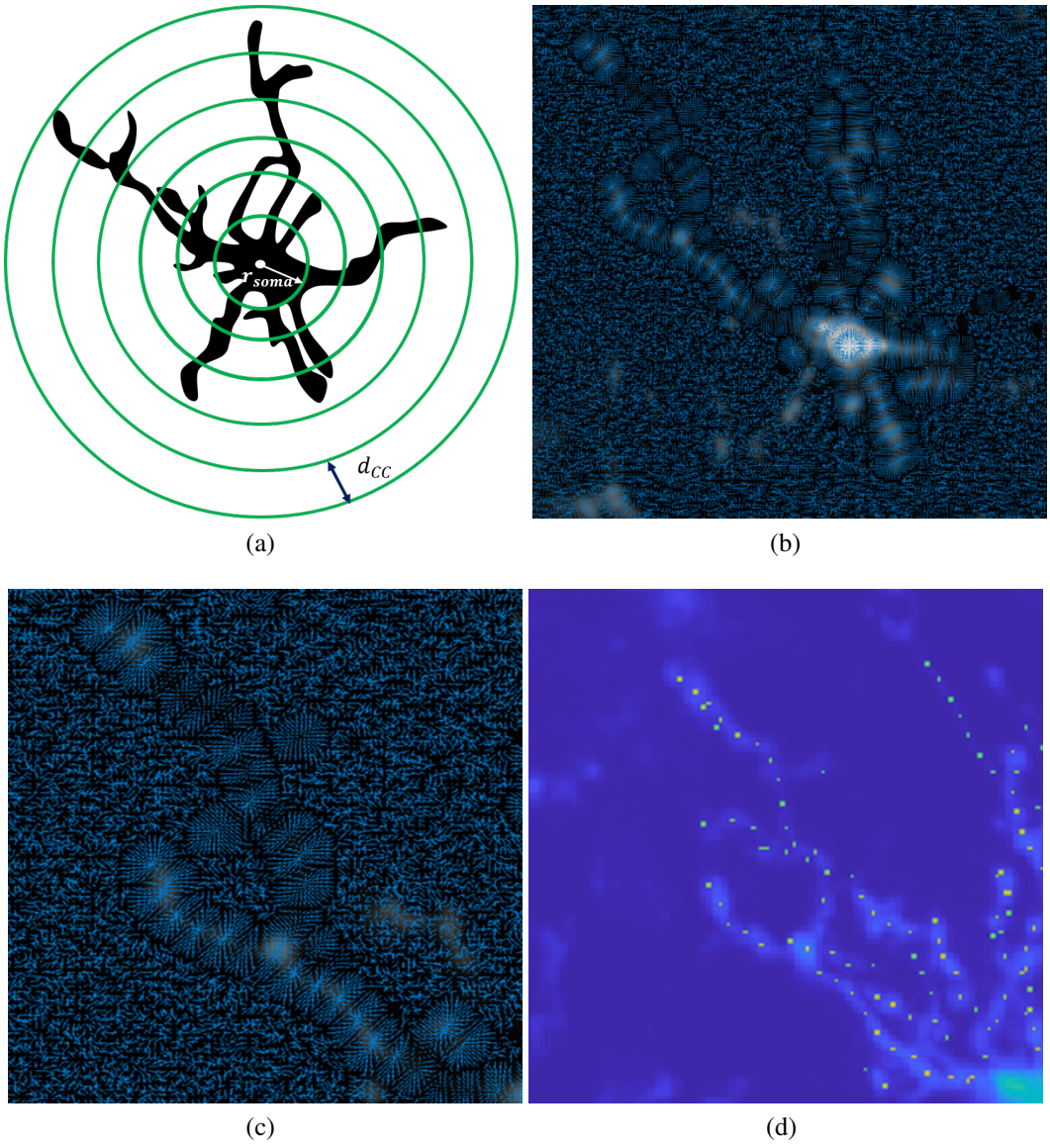

Figure 3.13: The VFC fields to find critical points of an object. **(a)** Concentric circles are placed around every detected soma to find **(b)**the vector field of the intensity image on these circles **(c)** zoomed in **(d)** the critical points on the object of interest.

These points do not form a continuous tracing of the glia but they lie on the centerline. The rest of the time arrival map is formed with the distance transform of the initialized seeds in Section 3.4.1.1. The fast marching algorithm computes the fastest path to get from one point to another.

For every object detected in the image, the critical points are a set of points on the centerline that will be traced back to the soma. We start with the farthest critical point from

Algorithm 1 Procedure for *C3VFC* for tracing medial axis of glia

Input Original 3D Image I.
Output 3D traced image T, SWC files T_{SWC};
Parameters d_{CC}, r_{vfc}

procedure C3VFC(I, params)
    $Soma \leftarrow$ soma detection on I using BFF method;
    $I_{fore} \leftarrow$ find foreground objects from curvature information of I;
    for each soma s in $Soma$ **do**
        $S^s \leftarrow$ use **Eq. 3.13** to get concentric circles;
        $f^s_{vfcCC} \leftarrow$ calculate concentric circle constrained VFC field using **Eq. 3.14** ;
        $criticalPointsList \leftarrow$ update vertices $\mathbf{V}_{fore}$ from $I_{fore} > 0$ using **Eq.** 3.10;
        while $criticalPointsList$ not empty **do**
            $process \leftarrow$ trace critical point to soma using FM;
            $T^s \leftarrow$ update image with traced $process$
            $criticalPointsList \leftarrow$ remove $criticalPointsList$ on $process$;
        end while
    end for
    Transfer T to T_{SWC};
return
end procedure

the soma to traverse through the path. After every iteration, we remove points the lie on the traced path from the *critical point list*. Then, the next point farthest from the soma is traced back to the soma until there are no more critical points in the set.

The output of our tracing workflow is a skeleton image that can be represented in the SWC file format. (In this case, SWC is the concatenation of the last initials of the inventors of the format.) The SWC file is a standard format for biological images with tree structures and is widely used by neuroscientists. With the SWC format, each foreground traced pixel of the connected cell is saved in matrix format with seven fields: index number, structure type, three *x*-*y*-*z* coordinates, radius and parent connection node. Since our algorithm detects and reconstructs the soma, we have formatted the SWC file to save the entire soma as the root node for accuracy. Typically the soma, or root node, is indicated by just the first row of the SWC file which is indicated by -1 as the parent connection node. Our SWC format saves all the soma voxels in the SWC file with a -1 as the parent connection node. Any child node of a soma voxel will indicate the index number as their parent connection node.

3.4.2 Experimental Results and Analysis

3.4.2 Imaging Acquisition and Fluorescence Technique

The multi-cellular dataset consists of 3D images of microglia from living mice using *in vivo* multiphoton microscopy, see supplementary materials SI2-SI4. Heterozygous GFP reporter mice expressing GFP under control of the fractalkine receptor promoter ($CX3CR1^{GFP/+}$) were used for the imaging studies. Wild-type C57/B6 mice were crossed with $CX3CR1^{GFP/GFP}$ mice from Jackson labs (Stock No. 005582) to generate $CX3CR1^{GFP/+}$ for these experiments to visualize microglia. For in vivo imaging, mice were implanted with a chronic cranial window as previously described [**bisht2020precise**]. Briefly, during surgery, mice were anesthetized with isoflurane (5% for induction; 1-2% for maintenance) and placed on a heating pad. Using a dental drill, a circular craniotomy of ¿ 3mm diameter was drilled at 2mm posterior and 1.5mm lateral to bregma, the craniotomy center was around the limb/trunk region of the somatosensory cortex. A 70% ethanol-sterilized 3mm glass coverslip was placed inside the craniotomy. A light-curing dental cement (Tetric EvoFlow) was applied and cured with a Kerr Demi Ultra LED Curing Light (DentalHealth Products). iBond Total Etch glue (Heraeus) was applied to the rest of the skull, except for the region with the window. This was also cured with the LED light. The light-curing dental glue was used to attach a custom-made head bar onto the other side of the skull from which the craniotomy was performed.

To label microglia in the mouse brain for the dataset in supplementary materials SI1, we used mice with an inducible Cre recombinase under the control of the CX3CR1 promoter crossed to the Ai6 fluorescent reporter mouse (Jackson Laboratories, Bar Harbor, ME) to generate $CX3CR1^{creERT2/+}$ X Ai6ZsGreen [42, 43]. At post-natal day (P23) 23, mice were given 10uL/g body weight of a 20mg/mL Tamoxifen (Sigma) solution in corn oil to induce recombination of the floxed stop codon leading to ZsGreen expression in microglia.

All procedures adhered to guidelines of the Institutional Animal Care and Use Committee

(ACUC) at the University of Virginia. Microglia of adult mice (7-10 weeks old) were imaged using a Leica TCS SP8 multiphoton microscopy system equipped with a Coherent Chameleon Ti:Sapphire laser and a 25x 0.95 NA immersion lens.

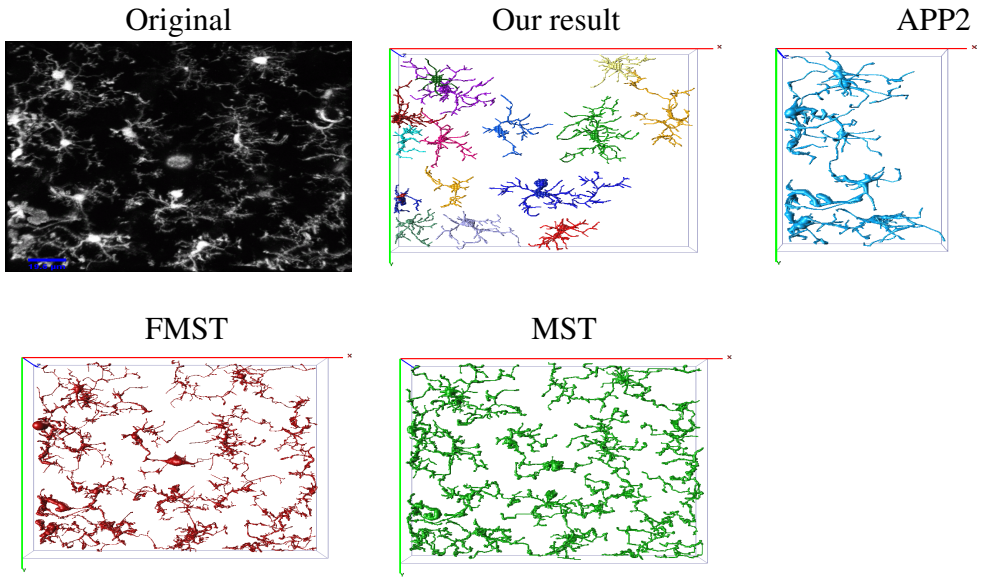

Figure 3.14: Visual comparison of the multi-cellular reconstruction results using C3VFC (our method), APP2, FMST, and MST. Traced foreground voxels are all non-black voxels.

3.4.2 Dataset

The multi-cellular 3D movies of microglia were imaged over 16 minutes taken at one minute intervals, containing multiple microglia per field of view. The 3D images were 1024 x 1024 x 61 pixels where the x-y frame was $295\mu m$ x $295\mu m$. For each image, there were 61 z-stacks acquired and the z-stack depth was taken in $1\mu m$ intervals. There are about 37 different cells in the multi-cellular video dataset, see supplmentary materials SI2-SI4. SI1-SI3 are microglia in *naive* mice, or mice that have not been previously subjected to experiments. SI4 is a video of the same microglia in SI3 that has been subjected to laser burn induced injury. The processing of 3D images is very difficult, because the varying intensity throughout the cell and non-structural noise along the z-stack make the actual cell signals hard to be visualized. To increase the intensity throughout the cell regions and the contrast of the images for further processing, histogram equalization was applied, although

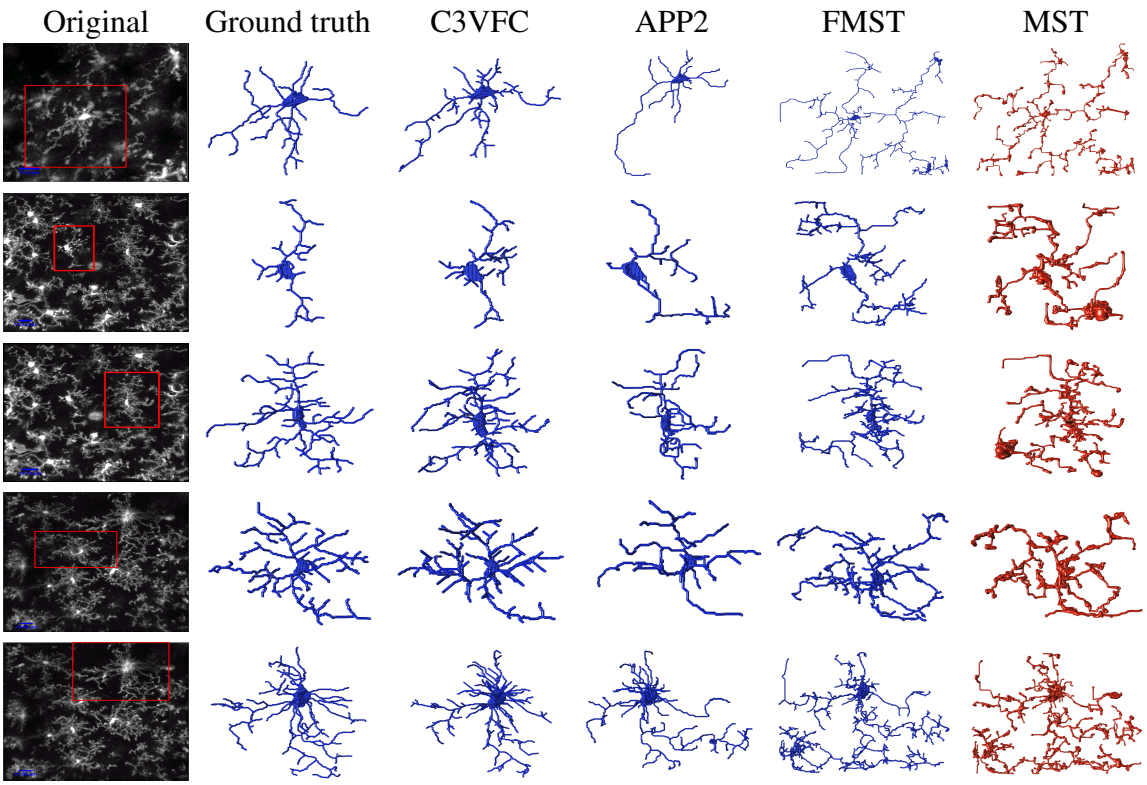

Figure 3.15: Reconstruction results of 3D microglia images. The first column on the left is the original image with the region of interest boxed out on the left. The following columns are the 3D reconstruction in SWC format.

some noise in the background may be increased too. The images were taken in naive mice and mice with laser burn induced injury that would vary the movement and morphology between the videos.

3.4.2 Performance Evaluation

We use datasets consisting of 3D images of microglia over a time of 16 minutes, as described in Section 3.4.2.2. We compare the temporal tracing results from C3VFC with results from state-of-the-art automatic skeleton reconstruction methods including improved all path pruning version 2 (APP2) [81], fast marching minimum spanning tree (FMST) [82], and minimum spanning tree (MST) [83]. APP2 is one of the fastest state-of-the-art methods for neuron tracing and has been used as the gold standard in some neuron reconstruction studies. APP2 is based on fast marching and hierarchical pruning and has proven that it can

achieve complete reconstructions for images with uneven pixel intensities, fine branches, and irregular sized cell bodies. We also compare our results with FMST and MST since both algorithms achieve higher or similar accuracy reconstruction scores than results from APP2 in numerous studies. MST uses local maxima to find points on the object of interest to create a minimum spanning tree to trace neurons. FMST is an advancement of the MST algorithm with the advantage of an over-segmentation and pruning method that is similar to that of APP2. The Vaa3D software was used to implement APP2, FMST, and MST. Vaa3D is short for 3D Visualization-Assisted Analysis software suite that is currently maintained and updated by HHMI - Janelia Research Campus and the Allen Institute for Brain Science [84]. For MST, the parameters for the window size were set to 10 or 15 depending on which value obtained a better result. The default settings for APP2 were used since they gave the best results. However, the output of the three comparison methods were insufficient for multi-cellular images. From the Figure 3.14, we see that APP2 could not detect over 50% of cells in a given image. Meanwhile, FMST and MST could not separate cells in a multi-cellular image. Thus, for the performance evaluation comparisons, each individual cell had to be manually cropped before inputting the image into APP2, FMST, and MST. *However, the entire multicellular image was input into C3VFC and output was the reconstruction image and SWC file format for all detected cells that were labelled over consecutive time frames.* The individual labelled glia were easily manipulated for comparison.

The accuracy of all the automatic reconstruction results are found against a baseline manual result. The baseline manual result is attained using the Simple Neurite Tracer in the ImageJ software [71]. The software allows for a semi-manual tracing setting in which the user could slide through the z-stacks of a 3D image and connect points along the branch paths. We note that the baseline manual result may have user error due to background noise and intensity inhomogeneity throughout the object of interest and through human error of estimating the centerline, especially through the z-stack view. The branch complexity of the cell and the resolution of the confocal microscope make it difficult to distinguish the path

of each branch and between cells that are in close proximity or touching. The 3D image captures a specific region of interest, so the soma of some branches may be occluded from the 3D image. Parts of some branches also extend outside the 3D image. These inevitable issues cause reconstruction error for both the automatic algorithms and the expert manual tracer.

Figure 3.15 shows the visual tracing results between the original image, the manual baseline, our result, and the result from the comparisons. Although C3VFC outputs the skeleton for all the cells in the entire image, individual cells are shown in the figure for a visual comparison against other methods. In our method, every cell is detected and labeled over time based off of the soma detection. This allows for a simple conversion from 3D skeleton image to SWC files and the extraction of image-based bioinformatics.

There is disagreement in the research community regarding how to evaluate the accuracy of a skeleton reconstruction. Manually tracing an object is indeed subject to intra-user and inter-user variability, especially in 3D, but such manual measurements represent the best existing choice for a baseline of quality. We use five different distance measures to measure the error between the baseline and the reconstruction results. We evaluate the performance of the reconstructions by measuring the average Euclidean distance between the reconstruction result and the ground truth. We input the SWC format reconstructions into Vaa3d to measure the entire-structure-average from 1 to 2 (ESA_{12}), ESA from 2 to 1 (ESA_{21}), average-bidirectional-ESA (ABESA), difference-structure-average (DSA), and percentage-of-different-structure (PDS), which were introduced and defined in [84]. $ESA_{12}$is a measure of the distance of a voxel from the ground truth to the closest voxel on the reconstruction result. ESA_{21} is a measure of the distance of a voxel from the reconstruction result to the closest voxel on the ground truth. $ABESA$ refers to the smallest spatial distance of a voxel between the reconstruction result to the closest voxel on the ground truth. DSA refers to the average spatial distance for the voxels that are different between the reconstruction result and the ground truth result. PDS is the percentage of the

voxels that are different between the reconstruction result and the ground truth result. We used the default two voxel spatial distance to account for human error and shown in [84] this value has a visible deviation. Table 3.1 shows the average and standard deviation of these distances compared with the manual baseline result. A lower value for each of these distances signify higher accuracy measure to the ground truth.

C3VFC has a lower error in all of the measures compared to APP2, FMST, and MST. APP2 achieved the second closest distance for four of the five measures: ESA_{21}, $ABESA$, DSA, and PSA. FMST and MST have a low ESA_{12} but higher ESA_{21} values signifying that their reconstruction contained a larger amount of false positive branches. FMST and MST also had the largest PDS values which tells that these reconstructions were the most different to the baseline reconstruction. The visual testimonial can be seen in Figure 3.15 where FMST and MST capture erroneous branches and noise that do not belong to the cell of interest. APP2 showed the most competitive results for all scores but it seemed to have missed the shorter processes and may over-prune its segmentation results. It must be noted that APP2 did not perform well when the entire multicellular image was input into the algorithm, as shown in Figure 3.14. FMST and MST seemed to be an over-segmentation, which was posed as an advantage of their algorithms, but the pruning was insufficient for glial images. From Table 1, if we consider the mean distance measure with the standard deviation, C3VFC achieves the best performance in four of the five accuracy measures: ESA_{21}, $ABESA$, DSA, and PSA. The mean distance measure with the standard deviation requires adding and subtracting the standard deviation from the mean to find the range of distance measures. C3VFC found up to a 53% improvement compared to APP2, FMST, and MST using the five accuracy measures (ESA_{12}, ESA_{21}, $ABESA$, DSA, and PSA). This percentage was attained by calculating the improvement of the worst distance measure for C3VFC over the next best distance measure in the comparison methods in Table 3.1. The worst accuracy measure for C3VFC was found by calculating the worst mean with the standard deviation of the measures. The worst performance for C3VFC would be for

ESA_{21}. This value is subtracted from the best performance measure for ESA_{21} achieved by the comparison algorithms, which was attained by APP2, to then find the percentage of improvement.

Table 3.1: Performance evaluation of results. The five measures computes the distance of the baseline manually traced results to the results from the respective methods. A lower value signifies better performance for all distance measures.

	C3VFC	APP2	FMST	MST
ESA_{12}	**3.85 ± 2.67**	6.18 ± 7.80	**4.60 ± .889**	4.92 ± 1.08
ESA_{21}	**7.77 ± 5.95**	15.4 ± 13.7	29.6 ± 27.23	33.4 ± 28.5
ABESA	**5.81 ± 3.64**	10.8 ± 7.71	17.1 ± 13.6	19.2 ± 14.2
DSA	**7.93 ± 4.066**	13.1 ± 8.76	18.0 ± 14.2	20.3 ± 14.7
PDS	**0.614 ± 0.124**	0.779 ± 0.114	0.890 ± .028	.899 ± 0.0197

The standard deviation in the measures for C3VFC could partially be attributed to the algorithm capturing parts of another cell, as shown in the temporal visualization in Figure 3.16. Since our method takes in the entire image with multiple cells, the accuracy is attributed to detecting the correct number of somas and cells. However, the 3D images may capture some processes with their corresponding soma outside of the 3D image, thus these processes may not be traced or erroneously picked up by another cell. Additionally, our method attempts to prevent capture of erroneous branches with the vector field, but some branches are touching and make it difficult to separate even with the human expert's eye. C3VFC intentionally does not trace branches with a corresponding soma not in the field of view. The purpose of the C3VFC algorithm is to trace temporal images for dynamic microglia analysis, and so, lone branches are considered to be background objects.

Figure 3.15 shows the visual tracing results between the original image, the manual baseline, our result, and the result from the comparisons. Although C3VFC outputs the skeleton for all the cells in the entire image, individual cells are shown in the figure for a visual comparison against other methods. In our method, every cell is detected and labeled over time based off of the soma detection. This allows for a simple conversion from 3D skeleton image to SWC files and the extraction of image-based bioinformatics.

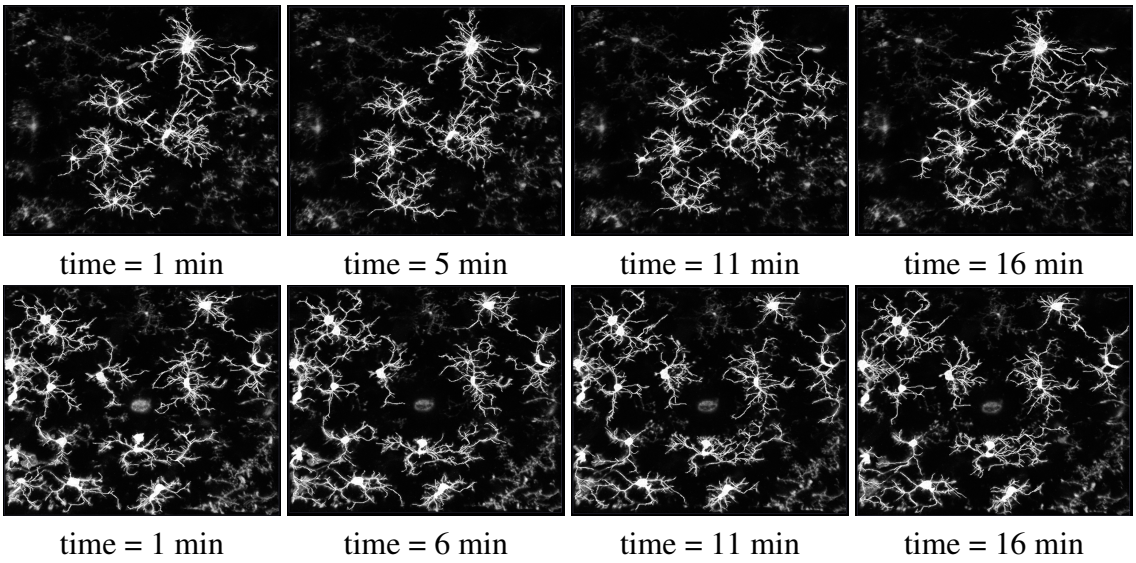

Figure 3.16: Reconstruction results of 3D microglia images over time. The video of the reconstruction results for the top and bottom rows could be found in Supplementary Information materials SI1 and SI4, respectively.

3.4.2 Measuring Tracing Consistency

The temporal tracing result using our method is attached as a video in the supplement. The video demonstrates the consistent tracing result over time and fluidity of motion. Consistent temporal tracing is imperative for accurate motility and morphology analysis. Consistency in this context means the reconstruction results and accuracy are agreeable over time. For example, correspondence between branches would be necessary to find the change in length or the velocity of a branch path over time. Figure 3.16 depicts snapshots of the 3D traced image over a few time points.

We measure consistency over consecutive time by calculating the average of the standard deviation of the measures between each frame. The consistency results are shown in Figure 3.17. The five measures describe the differences between the reconstruction results and the baseline result. Therefore, the standard deviation between the measures over time frames show how similar the results are over time. The results from C3VFC, FMST, and MST show a low average standard deviation which means the results show a high level of consistency among the time frames. FMST and MST results are consistently over segmented which

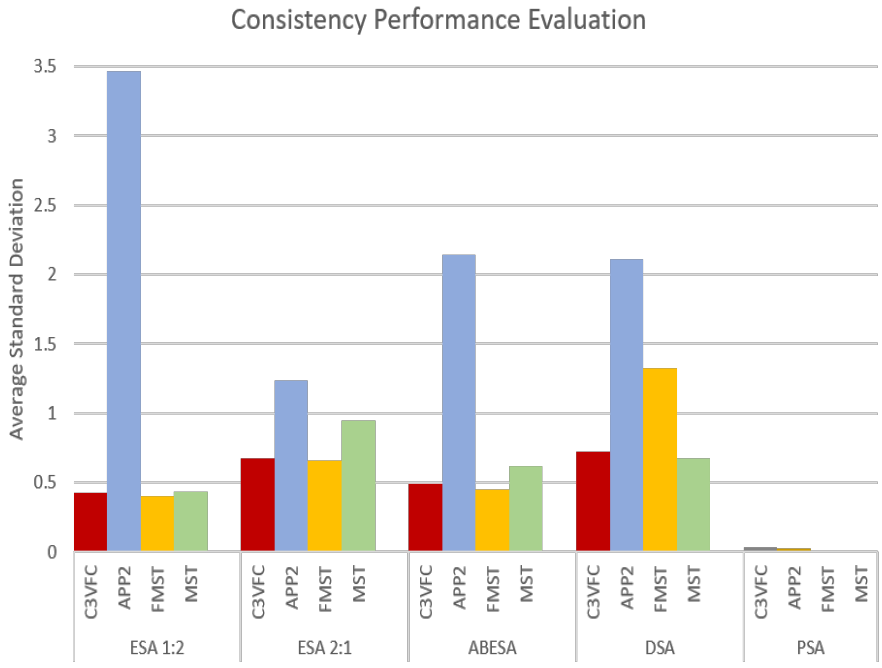

Figure 3.17: Consistency measure for the reconstruction results over time. We compare the standard deviations over time of the five performance measures (ESA 1:2, ESA 2:1, ABESA, DSA, PSA) for each of the reconstruction algorithms (C3VFC, APP2, FMST, MST). A lower average standard deviation constitutes a more consistent change over time. The scale for the PSA graph is from 0 to 1 because the PSA is a percentage.

could be a desired attribute. With C3VFC, the results consistently achieve a low mean square error for all of the five measures over 16 time frames.

3.5 Remarks

In this section, we propose the C3VFC algorithm for tracing and labelling 3D multi-cellular images of glia over consecutive time frames. In summary, the method followed the sequential steps: soma detection, critical point detection, and centerline tracing. C3VFC utilizes **v**ector **f**ield **c**onvolution in conjunction with constrained **c**oncentric **c**ircles to easily find the **c**ritical points that lie in the centerline of the glia processes. The critical points are traversed back to the corresponding soma to trace the glia processes. The output of the algorithm is the microglia reconstructions of a multi-cellular image that is labelled over time frames. The labelled reconstruction results could be individually analyzed over time in a SWC format.

We proved the efficacy of the reconstruction results with bioinformatics we developed to explain motility and morphology changes of microglia which can be used to analyze cells in different environments. The bioinformatics we provided included two ramification indexes, a skeletal growth index, and structural graph representation. Our contributions for a microglia reconstruction algorithm and accompanying bioinformatics were motivated by its desire in current literature and our collaborators in the neuroscience field.

In the experiments, we proved significant accuracy results and consistency of the C3VFC reconstruction results over consecutive time frames. We used datasets of 3D multi-cellular microglia images over 16 time frames. These 3D muli-cellular images over time were input into the C3VFC algorithm, while the individual cells had to be manually cropped before inputting them into the state-of-the-art methods that were used for comparison. Even so, in all of our experiments, C3VFC achieved a significantly higher accuracy measure to the manual baseline than all other methods in ESA_{12}, ESA_{21}, ABESA, DSA, and PDS. We define *significant* as having a lower mean square error average with standard deviation than the next best score. We generated the highest accuracy on the temporal microglia datasets, with up to 53% improvement over the next best reconstruction result. we also test the consistency of the reconstruction results to prove that C3VFC consistently achieves accurate results for all five measures over time frames. This proves that C3VFC could correctly trace the centerline and achieve better reconstruction results. We also proved the efficacy of our workflow since the microglia reconstructions were labeled over time - we showed that dynamic image-based bioinformatics could be extracted and can used for comparison of cells in different environments.

There are some limitations to C3VFC. In 3D images, portions of the cell could be exist outside of the field of view. A sufficient amount of erroneous tracing of branches happen in cases where the soma body of a cell is outside the field of view but the processes are in the field of view. Still, C3VFC produces consistent tracing results of multiple microglia in the field of view over time frames that are easily manipulated for extracting image-based

bioinformatics.

CHAPTER 4
BIOINFORMATICS

In this chapter, we provide bioinformatics that can be computed from the 4D segmentation results from Tuff-Bff in Chapter 2 and the 4D tracing results from Hieroglyph and V3VFC in Chapter 3. The bioinformatics yielded from image analysis can provide descriptive morphological and motion information in different settings. Time lapse analysis is imperative for studying the effects of microglia in brain development, reacting to an injury to the brain, or in diseased settings. First, we give a background on the analytics that have been used in literature by neuroscientists. Then, we provide novel set of bioinformatic tools specific to microglia motility and morphology. Some metrics may be useful in explaining microglia in different experimental settings and could possibly be used to classify microglia. In order to classify objects in different settings, we must determine features or measures that are significant and separable. We compare and analyze many different bioinformatic measures for microglia in different settings.

4.1 Background on microglia bioinformatics

A few groups have studied microglia movement by estimating the *rate of change of microglial processes*. Some estimated this bioinformatic measure by subtracting the number of pixels between consecutive images, where added or lost pixels were proxies for process ramification or extraction [85, 8]. This rate of change of the processes has been calculated by taking the average movement of the cell processes. Current ways of calculating the bioinformatic is thus measuring two different things. Further, calculating the change in number of pixels between frames may not necessarily be calculating branch ramification since the change in number of pixel could partially be accounted for by the change in process thickness over time or by movement of the entire image plane.

Skeletonizing microglia is a common method to analyze morphology. A skeleton provides a way to measure the changes in ramification of microglia processes in different settings, particularly between microglia in animal models that are naive, injured, or infected. Studies have shown that microglia ramification change in different settings which have previously been analyzed by finding the number of branches and process length [86, 87, 85]. One method of attaining a skeleton is described in [28] where the maximum intensity projection in the z-stack was binarized, skeletonized and analyzed using the AnalyzeSkelton function in ImageJ to find the number of endpoints and the process length. In [85], the authors additionally found the *tree branch area*- "area circumscribed by the polygonal object defined by connecting the outer points of the dendritic ramified arbor", *total dendritic length* - sum of all dendritic segments identified in a skeletonization of the arbor, and *total branch point number*- sum of branch points identified in a skeletonized rendition of the arbor.

Skeleton reconstructions provide a myriad of additional features and morphological information. In [36], the authors used their skeleton reconstruction to analyze the morphology of microglia following a ischemic stroke, a brain tissue injury. Some features they measured included the *sphericity* (compactness of the cell in 3D), *circularity* (compactness of the cell in 2D), *volumeP75* (volume of nodes; 75th percentile),*nodes total*, *branching nodes*, *end-nodes*, *nodes in branches*, *nodes per branch*, *end-nodes per branch*, *branch segments*, *segments per branch*, and *branch cycles*. Authors of [88] also studied the ramification of microglia using a rat model of aseptic neuroinflammation. They measured 15 features using *FracLac* for ImageJ, a free NIH-distributed software. These features included *fractal dimension* (to measure complexity), *lacunarity* (which measures heterogeneity or translational and rotational invariance in a shape), *cell area*, *convex hull area*, *density*, *cell perimeter*, *convex hull perimeter*,*roughness* (ratio of cell perimeter to convex hull perimeter), *convex hull span ratio* (the ratio of the major to minor axis), *cell circularity* $(4\pi cellarea)/(cellperimeter)^2)$,

Sholl analysis is a method to quantify dendritic arbors and does not fully depend on the accuracy of a segmentation or reconstruction method to attain an accurate analysis. Sholl

profiles plot the intersections of branches and the radial distance from the soma [89]. Some studies have used Sholl analysis on microglia images to find the process maximum (the maximum number of intersections for the cell), the critical value (the distance from the soma where the maximum number of intersections occurred), the maximum branch length (the maximum radius at which a branch intersection occurred) and the number of primary branches (the number of branches that originated from the microglia soma) [28]. Further, a Shoenen ramification index can be attained from this analysis by calculating the process maximum over the number of primary branches [90, 91, 36].

From the resulting reconstruction of our segmentation and skeletonization algorithms, we want to extract bioinformatic measures that could describe and quantify the activity of glia processes in different settings. In resting state, the microglia processes are ramified and are constantly surveilling the environment by extending and retracting their processes. Previous works have either manually or used a semi-automatic algorithm to measure process extension and retraction and process velocity [25, 26, 27, 28, 30, 31]. These works analyze each process individually. Our segmentation and skeletonization algorithms produce full 3D reconstructions. The goal is to use these digital representations to automatically extract process length, velocity, and other metrics that could characterize glia in different settings.

Scientists are trying to extract a rich set of image-based features in order to understand the relationship between the structure and function. The goal is to find discriminant features the can classify structurally different microglia. *In this section, we aim to determine image-based bioinformatic measures that quantify the dynamic morphological changes of microglia in different settings*. In this section, we analyze and quantify the morphological changes over consecutive image time frames.

4.2 Representing Microglia as Graphs

Microglia are comprised of a soma and processes that extend from the soma. This cell structure could be represented as a tree, or an acyclic undirected graph [92, 93]. An acyclic

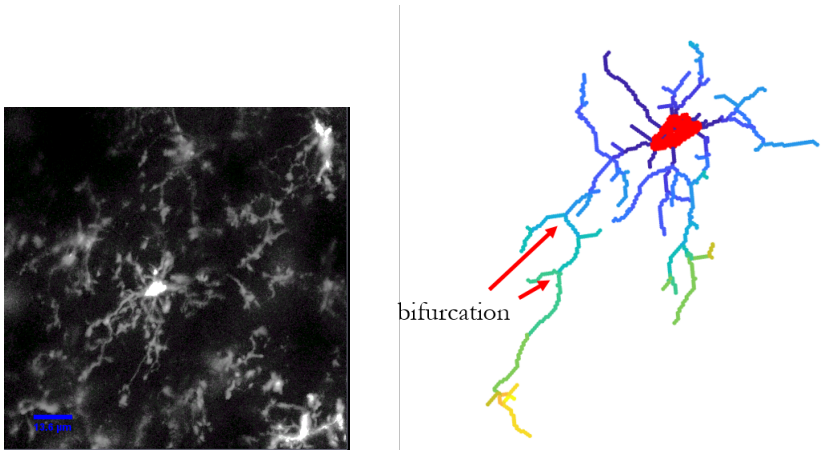

Figure 4.1: The original image of a microglia cell is shown on the left. The *glyph*, glia-graph representation is shown on the right. The path hierarchy is depicted by the different colors in the glyph. The paths hierarchy at each node is determined by the number of bifurcations that are crossed when traversed back to the soma.

graph is a graph with no loops. An undirected graph contains edges with no direction. Our method represents each foreground pixel in the traced skeleton as a vertex and is connected by an edge link, with a weight value of the Euclidean distance between connected pixels, where the graph is defined as $G = \{V, E, W\}$. We use the mathematical tree representation of the microglia to acquire structural information of the cell structure, such as the hierarchy, bifurcation nodes, and end nodes. A bifurcation occurs where the path divides into two parts. In microglia, the ramification and addition of new processes over time is telling of its environment and state. Microglia are highly ramified during active surveillance of surroundings. Such processes are less ramified, with fewer bifurcations, in a diseased setting, as described in Section 1.

Figure 4.1 depicts a microglia represented as a tree, with different colors representing different levels of hierarchy of the paths. The path hierarchy of a vertex is defined in [94] as the number of bifurcations that is crossed when traversed back to the root node, or the soma. The paths closest to the root node will have a value of one and the hierarchy number increases with additional bifurcations away from the soma.

4.3 Bioinformatic Analysis

The project discussed in this dissertation is motivated by the needs of neuroscientists in the Brain, Immunology, and Glia Center at UVA and those of the greater glia research community. The main question we want to answer is *what does microglia morphology reveal about the function of microglia?* To answer such a question, neuroscientists want to specifically know 1) the surveillance changes and 2) ramification changes over time.

Tracing consistent skeletons over time is a first step in analyzing microglia morphology in different scenarios. There is still much unknown about the role of microglia in different settings, particularly with respect to neurodegenerative disease. It is known that the morphology and motility of microglia changes in these diseased states. This section describes how our temporal tracing result from Hieroglyph and C3VFC can be used to analyze dynamic behavior of glial cells.

The swc (format) file of the digital reconstruction gives the spatial location of every pixel of the skeleton and the connections and relationships between all the pixels. Some features that could be attained from this graph representation include the branch lengths, the bifurcation points and angles, the end points of each branch, and hierarchy of the branches. From the branch length over time we could simply compute the branch velocity within each processes as well. Unlike previous studies, our method would extract informatic measures from the processes of the entire glia in 3D. Using these informatic measures, we propose to create quantitative descriptors of the 3D images of glia that could measure the movement of glia processes over time.

4.3.1 Surveillance

The surveillance can be determined by finding the volume change over time. It can also be thought of as the total volume covered in a space by the branch processes. This concept is useful to differentiate how much space the processes are surveilling in different settings.

Automatically quantifying surveillance of microglia is first addressed in Chapter 2. The coupled Tuff-Bff algorithm automatically segments 3D images of microglia. The results from these reconstructions are used to create metrics for quantifying microglia surveillance of its environments over time.

In Chapter 2 the results from the coupled Tuff-Bff segmentation algorithm are used to quantify surveillance over time. The volume of an object could be found by counting the voxels in the object. The foreground voxels of an object are given in the segmentation of the image.

From the segmentation result of coupled Tuff-Bff, as explained in Section 2, we separately but simultaneously segment the soma and processes. We are able to measure the volume covered by the processes over time, as shown in Figure 4.3. To attain the volume measure, we sum all the foreground pixels of the processes over time and convert this volume to cubic microns.

Neuroscientists are particularly interested in the total volume that the processes cover over time. This signifies how much of the environment the processes are surveilling in a given time, which also accounts for the process motility. The volume covered can be computed by finding the volume accumulated at each time frame. At the first time frame, the volume is computed by counting all of the foreground voxels. In the second time frame, the accumulated volume is the volume in the first time frame and any new voxels. In the third time frame, the accumulated volume is the accumulated volume from the second time frame (which is all foreground voxels in the first two time frames) and any new voxels not in the previous time frames. The remaining accumulated volume at other time points are computed the same way. The equation for computing the accumulated volume is:

$$accvolume_t = accvolume_{1:t} + (volume_t - (volume_t \&\& accvolume_{1:t}) \tag{4.1}$$

Figure 4.3 is a graph of the accumulated volume of processes over time of multiple

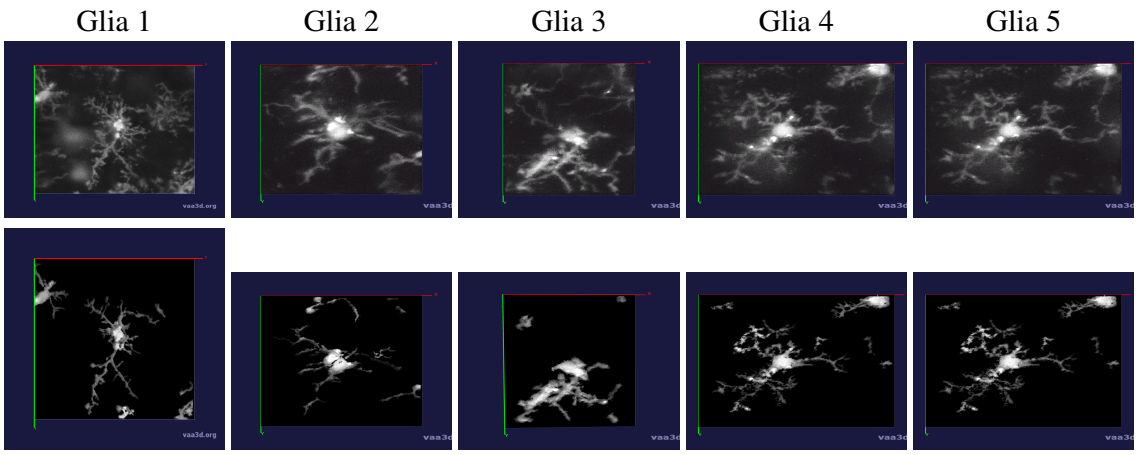

Figure 4.2: The images on the top row are the original images and the images on the bottom row are the segmentation results of 3D microglia images.

microglia from the image in Figure 4.2. The graph shows the accumulated volume covered over 13 minutes. The slope of this line is always positive or zero because it shows the rate at which new amount of space is covered.

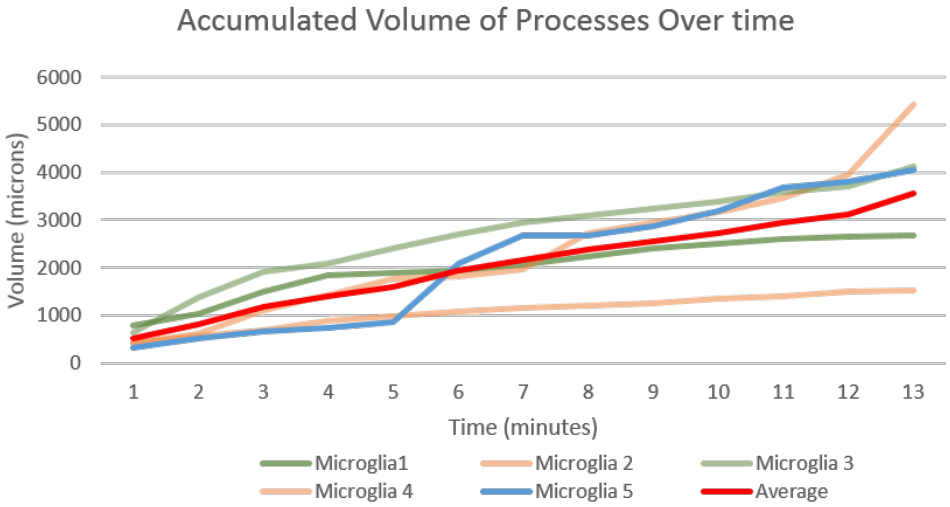

Figure 4.3: Accumulated volume of processes over time using the segmentation result from Coupled Tuff-Bff.

Figure 4.4 depicts the original and segmented 3D images of microglia from a healthy mouse and an infected mouse. Figure 4.5 shows the accumulated volume over time of the microglia in these images. The graph shows that the microglia from the healthy mouse surveys more of the environment over time than microglia in the infected mouse does. The

slope of each of the lines on the graph is the rate at which the processes covers space. The graph also shows that the total volume covered at each time frame is higher in the healthy mouse that in the infected mouse. From this volume graph we can conjecture information about the amount of space the processes takes up and velocity from the slope. It could be presumed that the processes of microglia from the healthy mouse are either longer or thicker than that of the microglia from the infected mouse. Information about how the microglia processes takes up that space would have to be described in other measurements.

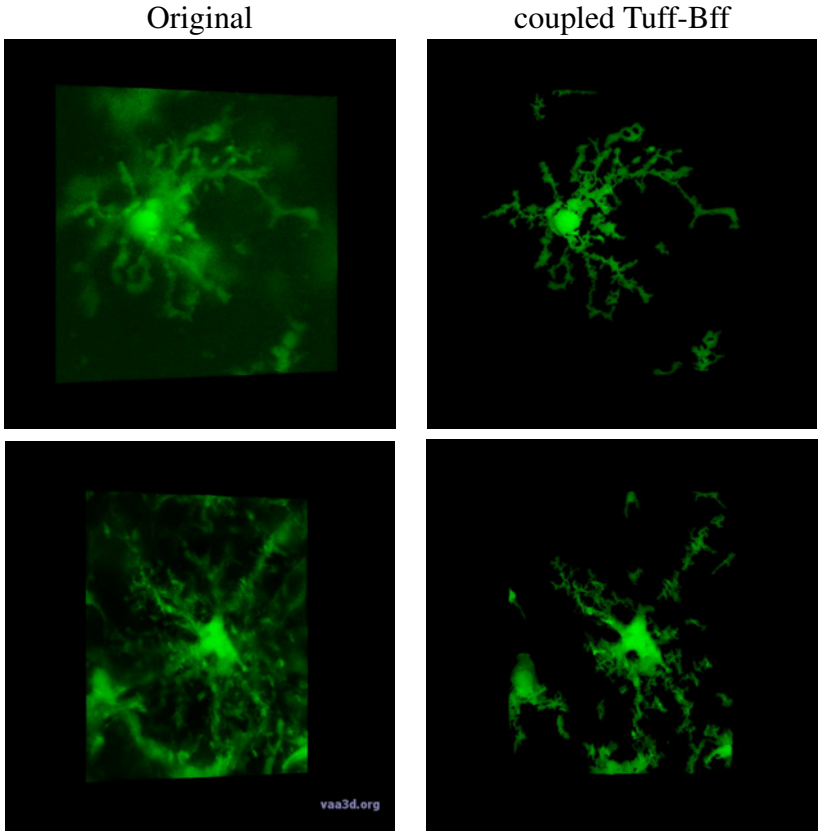

Figure 4.4: Segmentation results of microglia from healthy mouse (top row) and infected mouse (bottom row)

Madry *et al.* devised surveillance metrics for quantifying microglia that sums the pixels of processes that either extending or retracting between time frames [12]. This is index a good measure of changes between different frames, but their measurement is computed from the maximum intensity projection (MIP). The MIP projects the voxels with the highest attenuation on every view of the z stack of the volume onto a 2D image. Meanwhile

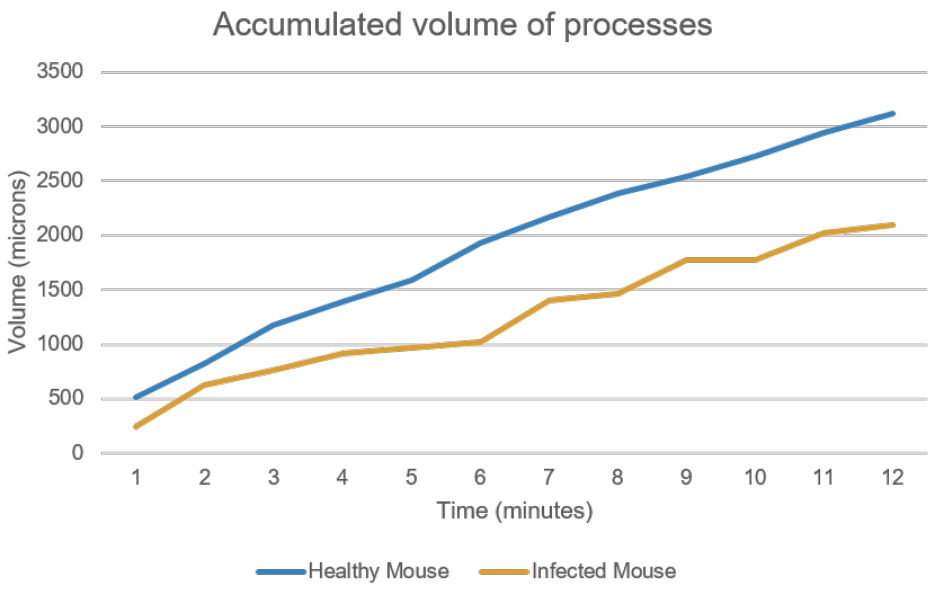

Figure 4.5: Volume of processes over time of healthy mouse vs. infected mouse.

the thickness, branch length, complexity of the branch, could be more telling of how the microglia takes up space and move. These measures would fall under ”ramification,” which describes the extension and retraction of microglia processes.

4.3.2 Ramification

Ramification changes over time details the amount of extension and retraction. Ramification is related to how much and how fast branches move over time. In terms of a quantifiable metrics, ramification can be quantified by finding the change branch length over time and branch velocity. The automatic skeleton algorithms in Chapter 3 aim to produce reconstruction results that will allow for quantifying dynamic bioinformatics regarding microglia movement over time. The skeleton along with swc reconstruction format allows for straightforward dynamic analysis. The skeleton is one voxel thick radius which makes finding the length of each length easier. The swc format stores the xyz location of every foreground voxel of the skeleton, radius, and parent voxel. This representation allows user to find more analytics related the the bifurcation, end points, and hierarchy of all the branches.

Determining the ramification of microglia processes requires finding the change in branch

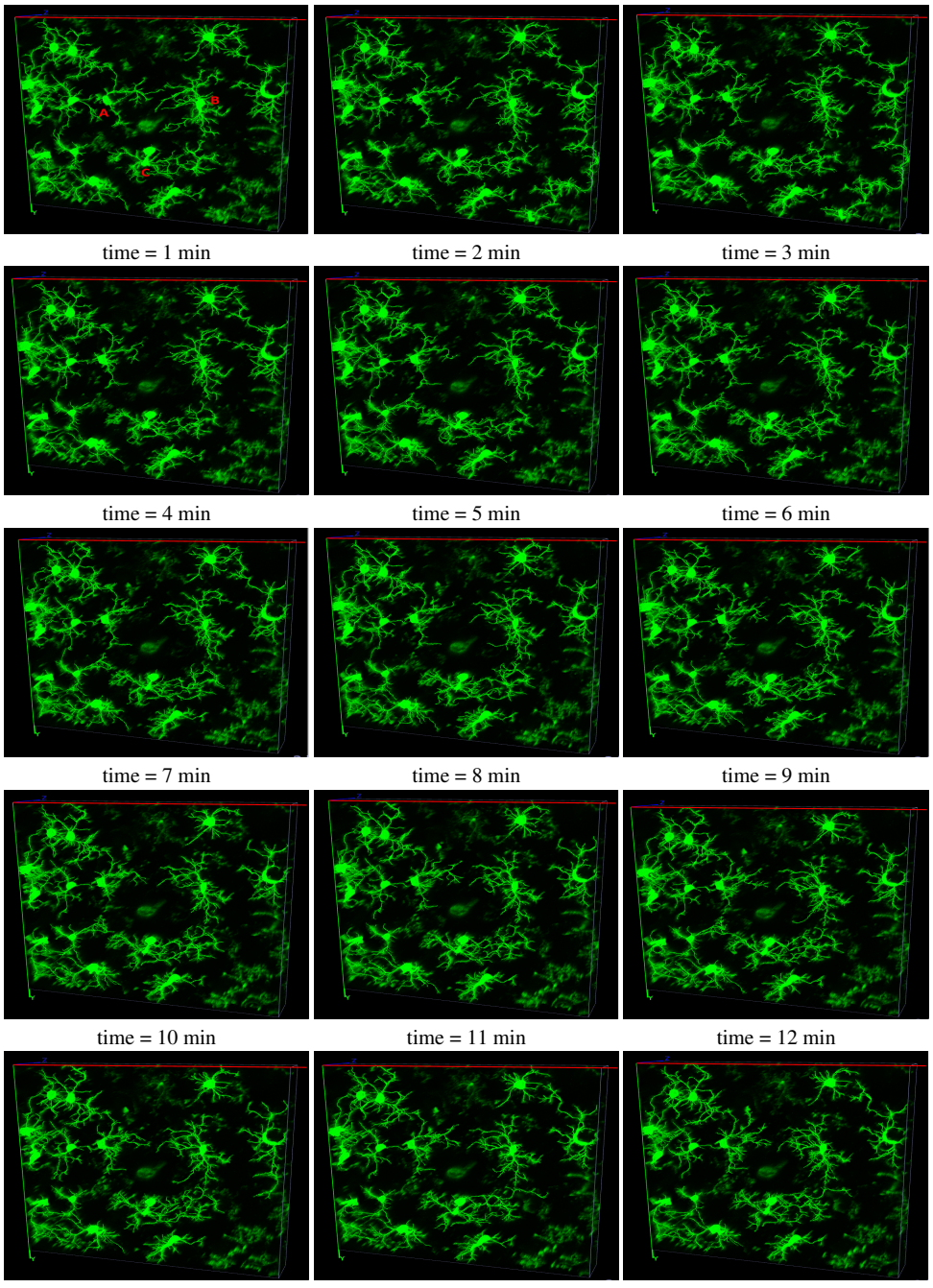

Figure 4.6: Segmentation results from C3VFC of microglia of a naive mouse.

length and motion over time. To automatically find the branch length the correspondence between the branches in each time frame must be known. Thus, we must emphasize that consistent reconstruction results from Chapter 3 is essential for this reason. Automatically detecting the correspondence of branches through time frames is a difficult task. Most

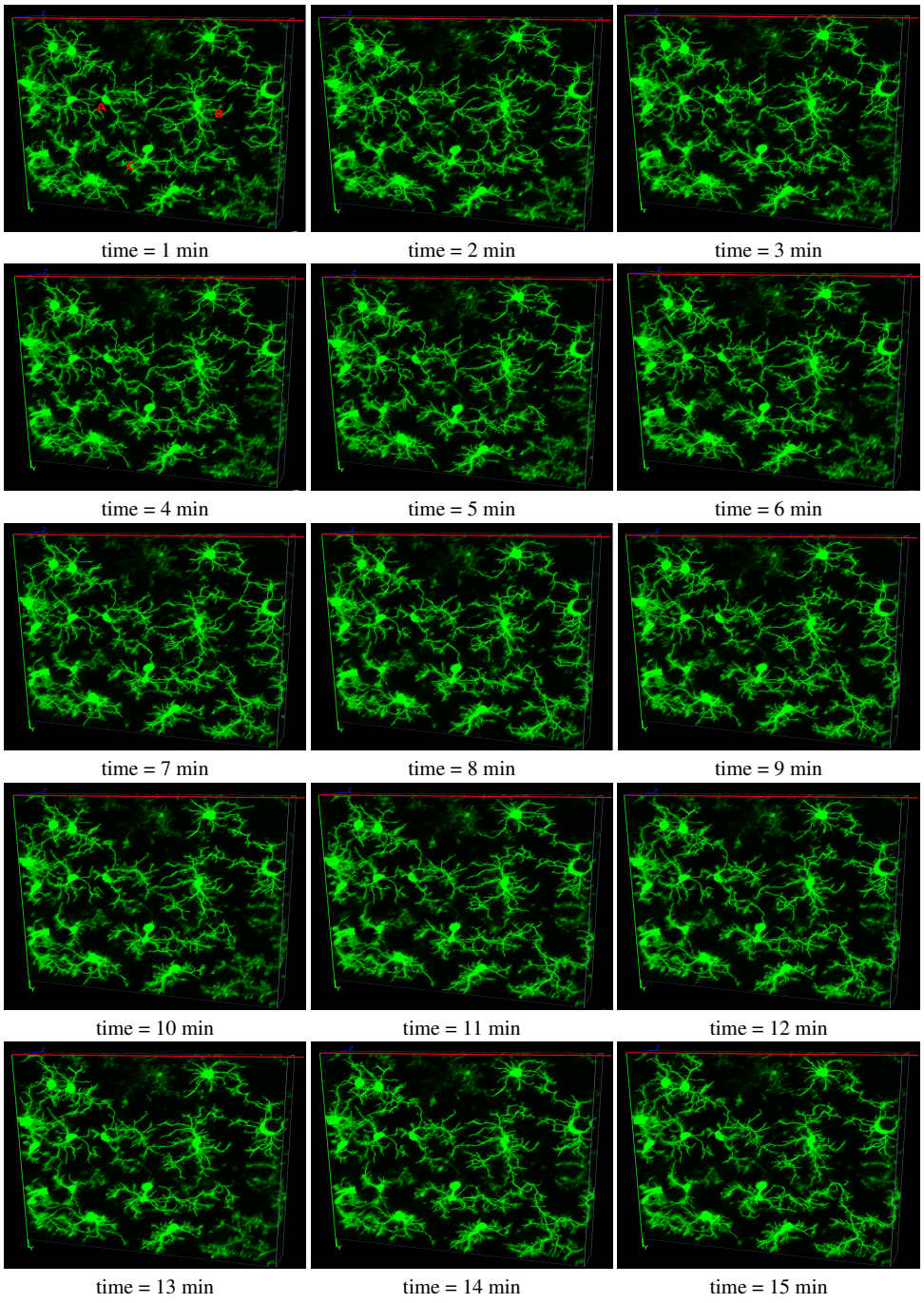

Figure 4.7: Segmentation results from C3VFC of microglia in a mouse brain with a laser-induced burn injury.

automatic ramifications measures are found globally, or the whole cell.

For this section, we compare the motility of microglia in naive mice and microglia in a brain with a laser induced injury. We show the visual tracing results produced from C3VFC in Figure 4.6 and Figure 4.7, respectively. It would be helpful to view the videos of these

results in the supplementary materials, labelled SI3 and SI4. The microglia in naive mice are moving at a continuous rate. It is clear that the microglia near the burn spot, labelled A, B, and C in Figure 4.6 and Figure 4.7, change their rate of motion. These microglia retract their processes before extending them towards the burn spot. Microglia A and B start to extend their processes towards the burn spot around the 6-minute mark, while microglia C starts extending at around 13 minutes.

We compute the average length of each path for a given microglia. A path traverses from an end point node back to the soma. The soma is labelled in our SWC file for each microglia, which makes it easier to find the start and end point of a path. As mentioned in Section 4.2, the graph representation of microglia allows us to find the hierarchy of each part of the processes. The SWC file stores the parent connection of each node so we can also find a bifurcation, a point with more than one child connection. We also know the end nodes which are the points with only one connection. With this information, we are able to differentiate the different paths. We find the length of each path and take the average of this length for each cell. The average path length of microglia depicted in Figure 4.6 and Figure 4.7 are shown in the graph in Figure 4.8. We can see from the graph the microglia from naive mice typically have a higher average path length. As we explained previously, the microglia in the brain with the burn injury are retracting its processes away from the burn spot. Madry *et al.* devised surveillance and ramification metrics for quantifying microglia [12]. Both indexes are measured for a 2D image of microglia, which in this case was the maximum intensity projection of the 3D image. The ramification index is the ratio of the perimeter to the area, as shown in Figure 4.9. As we can see from the figure, if the ramification index is R=1 then the cell is a perfect circle and there is no ramification. As the ramification index, R, increases the larger the processes ramification. The issue with this ramification index is, while it looks at the cell as a whole, it only take into account the most ramified processes and does not look at individual or the average processes. Our goal is to create a ramification and surveillance metrics that takes into account all the branch information in the 3D image.

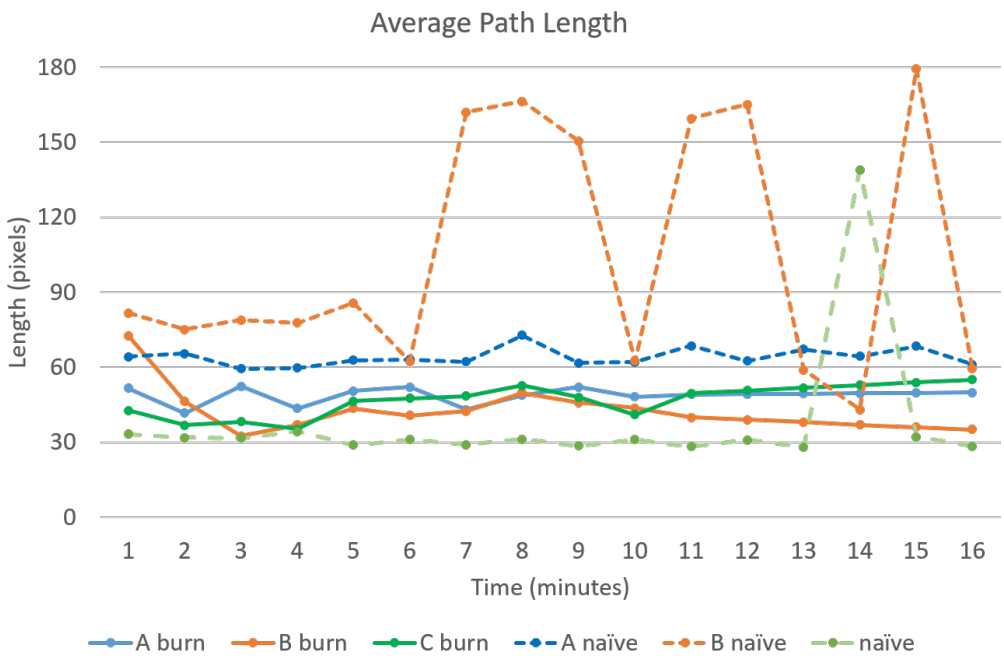

Figure 4.8: Average path length of microglia in naive mice and mice with a laser-induced burn spot.

Table 2.4.1 from Chapter 2.4.1 shows the ramification index for nine different microglia cells for the different reconstruction algorithms.

In [95], the authors developed a ramification index to explain changes in microglia motility when microglia activation is inhibited. Their ramification index was a measure of the ratio of the cell's perimeter over its area and normalized to a circle of that area: $R = (perimeter/area)/[2(\pi/area)^{1/2}]$. If *R*=1, then the cell has no branches, and thus no ramification. This ramification index was used for the 2D maximum intensity projection of the image. From this, we develop a 3D ramification index that can also describe the changes in extension and retraction of the microglia processes in different settings. Our 3D territorial ramification index (TRI) is a measure of the ratio of the volume of the convex hull of the skeleton and the volume of the soma. The convex hull is a polygonal enclosure of the extension of the skeleton. The TRI measures the ramification of the cell as a whole. As seen

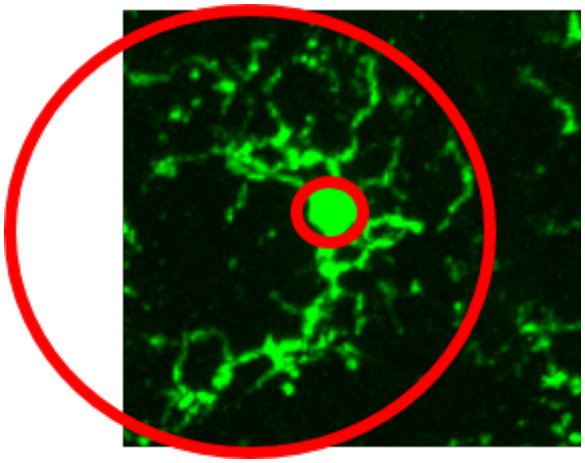

Figure 4.9: An illustration of the ramification index devised in [12].

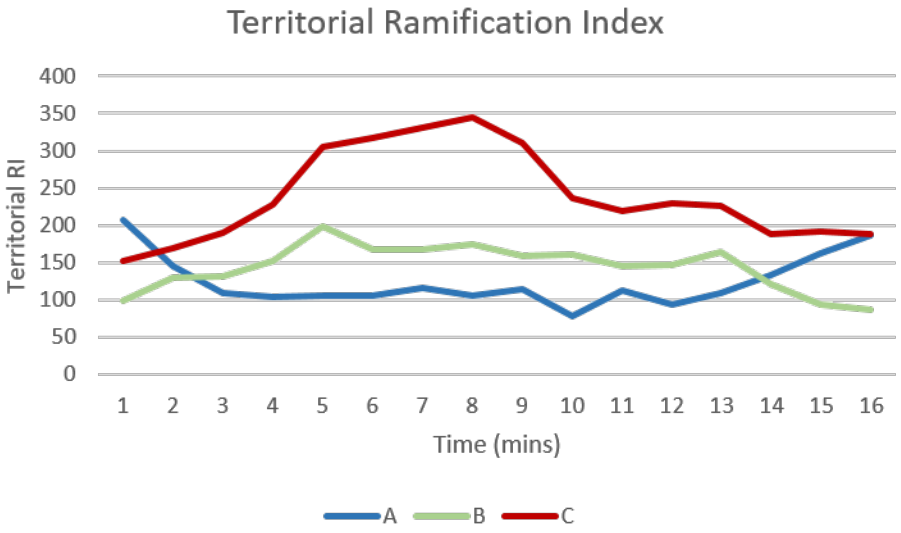

Figure 4.10: The graph shows the associated biofinformatic measures over time for three microglia labeled in 4.7.

in Figure 4.12, the processes of the microglia start to retract and then extends over time.

$$TRI = \frac{V_{convexhull}}{\|soma\|_0} \tag{4.2}$$

We also develop the skeletal ramification index which puts more weight on the individual branches. The SRI is the ratio of the volume of the skeleton and the volume of the soma. $SRI = 1$ indicates no ramification. From Figure 4.12, the cell labeled B may cover less

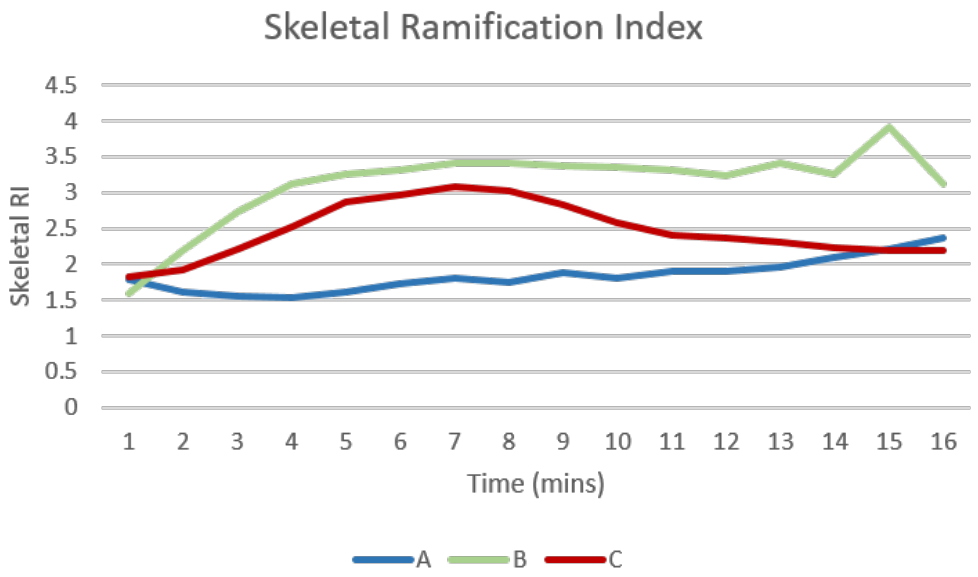

Figure 4.11: The graphs show the associated biofinformatics over time for three microglia labeled in 4.7.

territorial volume than glia C, but there is greater branch growth.

$$SRI = \frac{\|skeleton\|_0}{\|soma\|_0} \tag{4.3}$$

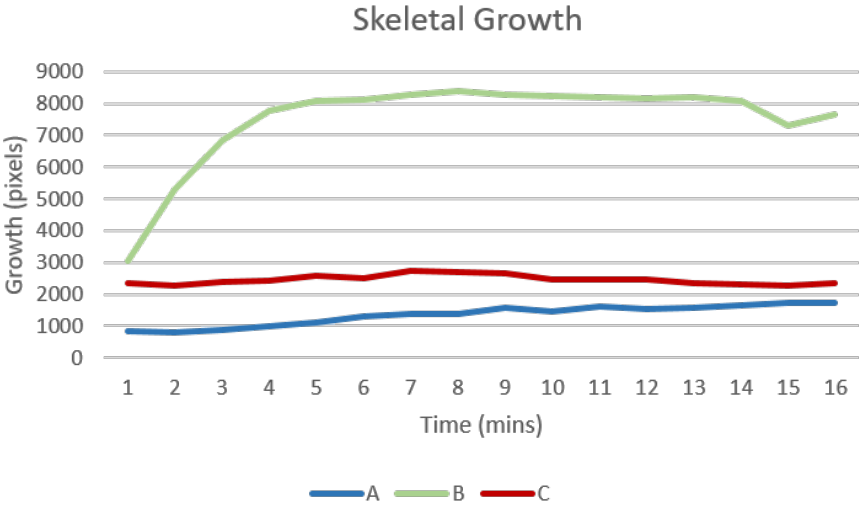

Figure 4.12: The graphs show the associated biofinformatics over time for three microglia labeled in 4.7.

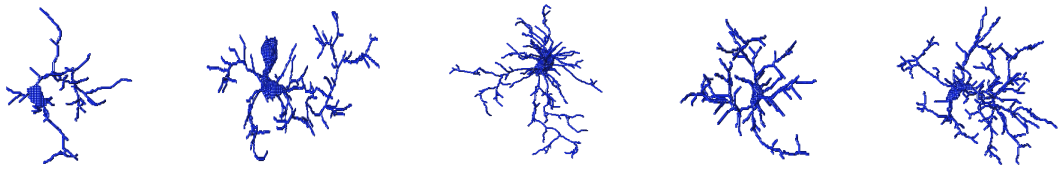

TRI	207.6	170.0	140.3	169.9	204.9
SRI	1.78	1.58	1.32	1.72	1.61

Figure 4.13: Examples of the TRI and SRI measures with different microglia.

From Figure 4.13, we show the TRI and SRI of five different microglia. The figure exemplifies that the soma size effects the TRI and SRI indexes since it is normalized by the soma volume.

Lastly, we measure the skeletal growth by finding the skeletal volume over time. The skeletal volume is computed by counting the total number of voxels in the skeleton and subtracting the soma volume. The soma has such a large volume compared to the thinned processes that it would outweigh the effects of the process volume. Additionally, this skeletal growth represents how the processes are surveilling its environment over time. The slope of this line is the velocity that measures how fast the skeleton changes over time.

4.4 Remarks

We have explained how to use the segmentation results from the three algorithms from the previous chapters to attain image-based bioinformatics. The surveillance and ramification measures as well as the indexes were introduced to study the change of microglia morphology and motility. In the future, longitudinal imaging studies will help us understand how long it takes microglia to change morphology. These studies could also determine the percentage of cells that change morphology. The reconstruction results from Chapters 2 and 3 combined with the different surveillance and ramification measures will certainly be useful for such morphological studies.

CHAPTER 5
DISCUSSION AND FUTURE WORK

The history of imaging microglia dates back to the 1880s when Franz Nissl developed the Nissl staining technique that allowed scientists to visualize cells in the brain, including microglia. Since then many scientist have been trying to describe microglia morphology. The earliest drawing and descriptions have come from the founder of neuroscience, Ramón y Cajal, his student Nicolás Achúcarro, and thenAchúcarro's student Pío del Río-Hortega, all of whom gave different visual descriptions of microglia. A century later, we are equipped with advanced microscopy imaging techniques, genetic engineering techniques, and image analysis tools that allow us to acquire clearer images and videos of microglia in different settings. The recent rediscovery that the immune system and the brain are a connected system has pushed research to trying to understanding microglia and their relationship the neurodegenerative diseases and brain injuries. Modern biological image analysis tools and software has allowed us to analyze and quantify images and videos in different settings.

Recent microglia research is constantly shifting our understanding of microglia and their relationship to neurodegenerative diseases, aging, and injury. In the homeostasis, the thin processes extends from the cell body, or soma, and is constantly surveilling its environement. However, in some settings, such as in a subject with Alzheimer's disease, some microglia in that environment change their morphology where the soma is more amoeboid shape and its processes are retracted. Microglia is the first cell that responds in brain injuries. This reaction is apparent in the morphological changes some microglia undergo during activation- from the thin, highly motile processes to an amoeboid cell. In other settings, scientists have found that microglia also change into other morphological shapes in different environments. Neuroscientists are trying to understand the relationship between these structural changes and their function or effect in different environments. Microglia imaging

has helped scientists quantify morphological changes. However, the quality of microscopy images, microglia's complex structure, and the myriad of morphological changes are a few of the challenges we face during microglia image analysis and morphological quantification.

In this dissertation, we utilize experts in the neuroscience domain to create an engineering solution that would help analyze microglia morphology. Neuroscientists have been trying to research *what micorglia structure can reveal about its function.* The two main things neuroscientists want to quantify is how surveillance and ramification of the processes change when microglia are in different environments. From an image processing perspective, we can answer these questions by designing an algorithm that will automatically segment the microglia over time. Bioinformatics related to surveillance and ramification, such as volume and processes length, can easily be extracted from microglia segmentation and skeletonization.

5.1 Segmentation

In the first part of this dissertation (Chapter 2), we present an automatic segmentation algorithm that is specific to reconstructing glial cells. Two-photon microscopy and advances in genetic engineering have allowed neuroscientists to image microglia in healthy environments or diseased and injured settings. We are able to observe how the morphology change in these different settings. However, microscopy images often exhibit background noise and clutter resulting from non-microglia fluorescence or artifacts. The processes of the microglia have smaller in radius and thus lower intensity than the soma does. The intensity varies along the processes, which makes it difficult to correctly reconstruct the processes to its corresponding soma. The question that the first part of this dissertation aims to solve is:

- finding a the segmentation result that could be used to find the changes in surveillance of microglia processes using 3D microglial images over consecutive time frames. Thus, the segmentation could be used to find the volume microglia processes cover over time.

In the following subsections we will summarize the each contribution to present the advantages, applicability and limitations of each technique.

5.1.1 Summary

The first algorithm, the coupled Tubularity flow field- Blob flow field (Tuff-Bff), provides an efficient way to simultaneously but separately segment the soma and processes of a microglia. The Tuff algorithm solved the issues of intensity imhomogeneity and disjoint segments for reconstructing the processes. The Bff worked to separately reconstruct the soma which is much larger and was rather blob-like unlike the processes. The couple Tuff-Bff algorithm ensures that there is not an overlap in reconstructing the soma and processes, rather it can distinguish between the two reconstructions. The first aim of microglia morpohology analysis is to quantify the surveillance of the processes. The coupled Tuff-Bff algorithm is valuable because:

- we have developed a method to segment microglia based on a geometric deformable model that is topologically adaptable.
- it can reconstruct the soma and distinguish from the processes. Soma detection is a major advantage in segmentation and is often times the first step in microglia reconstruction.
- it can separately segment the processes. The volume of the soma is so large that it overshadows the volume of the processes. We want to be able to understand how the processes move and take up space in its environment.

Observing the changes in soma and process morphology throughout different environments is key to quantifying microglia behavior. Both the soma and processes change their morphology depending on the environmental factor. However, the soma's size has a much greater volume than the thin processes that we would want to analyze the two separately. Further, soma detection in the coupled Tuff-Bff algorithm is a significant contribution of this

algorithm. We have shown in the following chapters that it was imperative for distinguishing the number of microglia and labelling the glia in images over consecutive time frames.

5.1.2 Future Work

The coupled Tuff-Bff algorithm is an essential contribution the segmentation of glial cells. However, this algorithm segments each time frame separately. It is shown in Chapter 3 that having consistent reconstructions over time is critical for morphology analysis. The coupled Tuff-Bff algorithm inputs a single image and outputs the reconstruction of that image. because of the intensity inhomogeneity throughout the processes and the changes in background clutter of the images between time frames, the reconstructions may be inconsistent over time.

5.2 Consistent reconstruction over time

The second part of this dissertation (Chapter 3) is focused on acquiring consistent reconstructions over consecutive time frames to evaluate the ramification of microglia in different settings. The aim of this section was to find a solution that will handle reconstructions of 3D microglia images over time that would guide bioinformatics analysis. The question that results in this section aims to answer is:

- the changes in ramification of microglia processes using 3D microglial images over consecutive time frames.

In the following subsections we will summarize the each contribution to present the advantages, applicability, and limitations of each technique.

5.2.1 Summary

The second algorithm, called *Hieroglyph*, hierarchically matches microglia graph to glia of subsequent time frames to produce microglia skeletons over time. *Hieroglyph* was

primarily designed to use temporal image information to generate consistent skeletons over subsequent time frames. Finding corresponding branches of microglia over time could facilitate quantifying motility of a glia. The contributions of this method are as follows:

- Providing a consistent temporal skeleton benefits the assessment of microglia motility in different environments
- The hierarchical matching of glia through temporal data allows us to find the correspondence between all the branches and its hierarchy

The issue with this method is that it relies on the segmentation of the glia in the first time frame. Further, new processes appear and disappear which may not be accounted for in subsequent time frames. *Hieroglyph* also inputs a 3D video with one microglia at a time. We develop another skeletonization algorithm that is able to accurately reconstruct 3D temporal images with multiple microglial objects. The contributions of *C3VFC* are as follows:

- processes are accurately traced back to its corresponding microglia using a novel technique that takes advantage of vector field convolution.
- soma detection allows for automatic reconstruction of multiple microglia in an image.
- soma detection allows for automatic labelling of microglia over subsequent time frames.
- the skeleton binary reconstruction is also represented compactly as a graph structure and facilitates extracting bioinformatic measures related to microglia morphology.

5.2.2 Future Work

We have presented two 3D reconstruction algorithms that have proven to attain consistent results over time. The first algorithm, Hieroglyph, used temporal information to skeletonize the cell, but it relied to much on the correct segmentation of the previous time. This method also introduces the mathematical representation of a glia as a *glyph*, or glia graph structure.

C3VFC was able to reconstruct multiple microglia within an image over time while also detecting and reconstructing the soma. Although C3VFC did not use temporal information to reconstruct the microglia, it did prove that the temporal reconstructions were consistent over time. However, the computational complexity of the algorithm could be improved. The algorithm had the longest computational time tracing the critical points back to the soma.

5.3 Bioinformatics

In the last part of this dissertation (chapter 4) we use the results from the reconstruction algorithms to extract useful bioinformatics information and compare microglia morphology in different environments. To reiterate, the goal of current research related to microglia is to understand the relationship of its structure to its function in different environments. It is apparent that microglia change morphology from its large soma and thin elongated processes to a less motile, amoeboid shape. Scientists are trying to understand the impact of these morphological changes effects on the brain environment. It is known that microglia is related to neurodegenerative diseases and brain injuries. Yet, there are still many questions that lead scientists to want to understand by quantifying their morphology. With the expertise and guidance of neuroscientists at UVa, we aim to establish a viable set of bioinformatics that may help understand microglia morphology and motility.

5.3.1 Summary

In the last chapter, we use the results from the three reconstruction algorithms to determine useful quantitative measurements and bioinformatics to determine surveillance and ramification of microglia.

- we compare surveillance metrics between microglia in a healthy mouse versus in a diseased mouse.
- we use the reconstruction results to generate bioinformatics such as branch length,

velocity, and different ramification indexes

- we use the graph representation of microglia to devise quantification tools.

5.3.2 Future Work

Microglia research is still at its genesis were advancements are being made every day. The current tools used by scientists to quantify microglia images is can still be improved. This dissertation provides a set of automatic reconstruction techniques for images of microglia. From an engineering perspective, the obvious research that should follow should be classification of microglia in different settings. However, more quantitative studies must be done before it is possible to classify microglia based off their morphology. Longitudinal studies would be useful for studying the rate of morphological change. The image-based bioinformatics measures examplified in this thesis could be used to study the microglia morphology and motion.

5.4 List of Publications

1. T. T. Ly, J. Wang, N. Tabassum, and S. T. Acton. ”Review on Level Set Methods in Biological Imaging.” Biological Imaging. *in progress* 2021.

2. T. T. Ly, J. Wang, K. Bisht, U. Eyo, and S. T. Acton. ”C3VFC: A Method for Tracing and Quantification of Microglia in 3D Temporal Images.” MDPI, Medical Image Analysis: From Small Size Data to Big Data. *in revision* 2021.

3. T. T. Ly, T. Batabyal, J. Thompson, D. Weller, T. Harris, and S. T. Acton. ”Hieroglyph: Hierarchical Glia Graph Skeletonization and Matching.” Asilomar, 2019.

4. T. Ly, J. Thompson, T. Harris, and S. T. Acton. ”The Coupled TuFF-BFF Algorithm for Automatic 3D Segmentation of Microglia.” In 2018 25th IEEE International Conference on Image Processing (ICIP), pp. 121-125. IEEE, 2018. . [pdf]

5. T. Ly, R. Sarkar, K. Skadron, and S. T. Acton, “Classifying Images in a Histopathological Dataset Using the Cumulative Distribution Transform on an Automata Architecture,” in Global Conference on Signal and Information Processing (GlobalSIP) , Nov 2017.

6. T. Ly, R. Sarkar, K. Skadron, and S. T. Acton, “Feature extraction and image retrieval on an automata structure,” in Proceedings of the 50th Asilomar Conferences on Signals, Systems, and Computers, Nov 2016. [pdf]

REFERENCES

[1] K. M. Lucin and T. Wyss-Coray, "Immune activation in brain aging and neurodegeneration: Too much or too little?", *Neuron*, vol. 64, no. 1, pp. 110–122, 2009.

[2] U. B. Eyo and L.-J. Wu, "Bidirectional microglia-neuron communication in the healthy brain", *Neural plasticity*, vol. 2013, 2013.

[3] M. Colonna and O. Butovsky, "Microglia function in the central nervous system during health and neurodegeneration", *Annual Review of Immunology*, vol. 35, pp. 441–468, 2017.

[4] D. P. Schafer and B. Stevens, "Microglia function in central nervous system development and plasticity", *Cold Spring Harbor Perspectives in Biology*, vol. 7, no. 10, a020545, 2015.

[5] P. L. Poliani, Y. Wang, E. Fontana, M. L. Robinette, Y. Yamanishi, S. Gilfillan, and M. Colonna, "Trem2 sustains microglial expansion during aging and response to demyelination", *The Journal of clinical investigation*, vol. 125, no. 5, pp. 2161–2170, 2015.

[6] J. C. Cronk, A. J. Filiano, A. Louveau, I. Marin, R. Marsh, E. Ji, D. H. Goldman, I. Smirnov, N. Geraci, S. Acton, *et al.*, "Peripherally derived macrophages can engraft the brain independent of irradiation and maintain an identity distinct from microglia", *Journal of Experimental Medicine*, vol. 215, no. 6, pp. 1627–1647, 2018.

[7] H. Wake, A. J. Moorhouse, S. Jinno, S. Kohsaka, and J. Nabekura, "Resting microglia directly monitor the functional state of synapses in vivo and determine the fate of ischemic terminals", *Journal of Neuroscience*, vol. 29, no. 13, pp. 3974–3980, 2009.

[8] M.-È. Tremblay, R. L. Lowery, and A. K. Majewska, "Microglial interactions with synapses are modulated by visual experience", *PLoS Biology*, vol. 8, no. 11, e1000527, 2010.

[9] D. Davalos, J. K. Ryu, M. Merlini, K. M. Baeten, N. Le Moan, M. A. Petersen, T. J. Deerinck, D. S. Smirnoff, C. Bedard, H. Hakozaki, *et al.*, "Fibrinogen-induced perivascular microglial clustering is required for the development of axonal damage in neuroinflammation", *Nature Communications*, vol. 3, p. 1227, 2012.

[10] F. Ginhoux, S. Lim, G. Hoeffel, D. Low, and T. Huber, "Origin and differentiation of microglia", *Frontiers in cellular neuroscience*, vol. 7, p. 45, 2013.

[11] I. Hristovska and O. Pascual, "Deciphering resting microglial morphology and process motility from a synaptic prospect", *Frontiers in integrative neuroscience*, vol. 9, p. 73, 2016.

[12] C. Madry, V. Kyrargyri, I. L. Arancibia-Cárcamo, R. Jolivet, S. Kohsaka, R. M. Bryan, and D. Attwell, "Microglial ramification, surveillance, and interleukin-1β release are regulated by the two-pore domain k+ channel thik-1", *Neuron*, 2017.

[13] J. C. Savage, M. Carrier, and M.-È. Tremblay, "Morphology of microglia across contexts of health and disease", *microglia*, pp. 13–26, 2019.

[14] N. P. B. Au and C. H. E. Ma, "Recent advances in the study of bipolar/rod-shaped microglia and their roles in neurodegeneration", *Frontiers in Aging Neuroscience*, vol. 9, p. 128, 2017.

[15] M.-È. Tremblay, C. Lecours, L. Samson, V. Sánchez-Zafra, and A. Sierra, "From the cajal alumni achúcarro and río-hortega to the rediscovery of never-resting microglia", *Frontiers in neuroanatomy*, vol. 9, p. 45, 2015.

[16] A. Sierra, R. C. Paolicelli, and H. Kettenmann, "Cien años de microglía: Milestones in a century of microglial research", *Trends in neurosciences*, vol. 42, no. 11, pp. 778–792, 2019.

[17] W. Spielmeyer, *Histopathologie des nervensystems*. J. Springer, 1922, vol. 1.

[18] C. Condello, P. Yuan, and J. Grutzendler, "Microglia-mediated neuroprotection, trem2, and alzheimer's disease: Evidence from optical imaging", *Biological psychiatry*, vol. 83, no. 4, pp. 377–387, 2018.

[19] Z. Shen, X. Bao, and R. Wang, "Clinical pet imaging of microglial activation: Implications for microglial therapeutics in alzheimer's disease", *Frontiers in aging neuroscience*, vol. 10, p. 314, 2018.

[20] A. Gerhard, N. Pavese, G. Hotton, F. Turkheimer, M. Es, A. Hammers, K. Eggert, W. Oertel, R. B. Banati, and D. J. Brooks, "In vivo imaging of microglial activation with [11c](r)-pk11195 pet in idiopathic parkinson's disease", *Neurobiology of disease*, vol. 21, no. 2, pp. 404–412, 2006.

[21] Y. F. Tai, N. Pavese, A. Gerhard, S. J. Tabrizi, R. A. Barker, D. J. Brooks, and P. Piccini, "Imaging microglial activation in huntington's disease", *Brain research bulletin*, vol. 72, no. 2-3, pp. 148–151, 2007.

[22] N. Otsu, "A threshold selection method from gray-level histograms", *IEEE Transactions on Systems, Man, and Cybernetics*, vol. 9, no. 1, pp. 62–66, 1979.

[23] S. R. y Cajal, *Degeneration & regeneration of the nervous system*. Hafner Publishing Company, 1959, vol. 1.

[24] D. E. Donohue and G. A. Ascoli, "Automated reconstruction of neuronal morphology: An overview", *Brain research reviews*, vol. 67, no. 1-2, pp. 94–102, 2011.

[25] A. Nimmerjahn, F. Kirchhoff, and F. Helmchen, "Resting microglial cells are highly dynamic surveillants of brain parenchyma in vivo", *Science*, vol. 308, no. 5726, pp. 1314–1318, 2005.

[26] L.-J. Wu and M. Zhuo, "Resting microglial motility is independent of synaptic plasticity in mammalian brain", *Journal of neurophysiology*, vol. 99, no. 4, pp. 2026–2032, 2008.

[27] D. Davalos, J. Grutzendler, G. Yang, J. V. Kim, Y. Zuo, S. Jung, D. R. Littman, M. L. Dustin, and W.-B. Gan, "Atp mediates rapid microglial response to local brain injury in vivo", *Nature Neuroscience*, vol. 8, no. 6, p. 752, 2005.

[28] H. W. Morrison and J. A. Filosa, "A quantitative spatiotemporal analysis of microglia morphology during ischemic stroke and reperfusion", *Journal of neuroinflammation*, vol. 10, no. 1, p. 782, 2013.

[29] S. Gyoneva, D. Davalos, D. Biswas, S. A. Swanger, E. Garnier-Amblard, F. Loth, K. Akassoglou, and S. F. Traynelis, "Systemic inflammation regulates microglial responses to tissue damage in vivo", *Glia*, vol. 62, no. 8, pp. 1345–1360, 2014.

[30] K. Young and H. Morrison, "Quantifying microglia morphology from photomicrographs of immunohistochemistry prepared tissue using imagej", *Journal of visualized experiments: JoVE*, no. 136, 2018.

[31] I. Paris, J. C. Savage, L. Escobar, O. Abiega, S. Gagnon, C.-W. Hui, M.-È. Tremblay, A. Sierra, and J. Valero, "Promoij: A new tool for automatic three-dimensional analysis of microglial process motility", *Glia*, vol. 66, no. 4, pp. 828–845, 2018.

[32] Y. Ding, M. C. Pardon, A. Agostini, H. Faas, J. Duan, W. O. Ward, F. Easton, D. Auer, and L. Bai, "Novel methods for microglia segmentation, feature extraction, and classification", *IEEE/ACM transactions on computational biology and bioinformatics*, vol. 14, no. 6, pp. 1366–1377, 2017.

[33] C. Kozlowski and R. M. Weimer, "An automated method to quantify microglia morphology and application to monitor activation state longitudinally in vivo", *PloS one*, vol. 7, no. 2, e31814, 2012.

[34] Y. Ding, M. C. Pardon, A. Agostini, H. Faas, J. Duan, W. O. Ward, F. Easton, D. Auer, and L. Bai, "Novel methods for microglia segmentation, feature extraction, and

classification", *IEEE/ACM transactions on computational biology and bioinformatics*, vol. 14, no. 6, pp. 1366–1377, 2016.

[35] S. Healy, J. McMahon, P. Owens, P. Dockery, and U. FitzGerald, "Threshold-based segmentation of fluorescent and chromogenic images of microglia, astrocytes and oligodendrocytes in fiji", *Journal of neuroscience methods*, vol. 295, pp. 87–103, 2018.

[36] S. Heindl, B. Gesierich, C. Benakis, G. Llovera, M. Duering, and A. Liesz, "Automated morphological analysis of microglia after stroke", *Frontiers in cellular neuroscience*, vol. 12, p. 106, 2018.

[37] N. F. Ash, M. T. Massengill, L. Harmer, A. Jafri, and A. S. Lewin, "Automated segmentation and analysis of retinal microglia within imagej", *Experimental Eye Research*, vol. 203, p. 108 416, 2021.

[38] M. Abdolhoseini, F. Walker, and S. Johnson, "Automated tracing of microglia using multilevel thresholding and minimum spanning trees", in *2016 38th Annual International Conference of the IEEE Engineering in Medicine and Biology Society (EMBC)*, IEEE, 2016, pp. 1208–1211.

[39] M. G. Kluge, L. Kracht, M. Abdolhoseini, L. K. Ong, S. J. Johnson, M. Nilsson, and F. R. Walker, "Impaired microglia process dynamics post-stroke are specific to sites of secondary neurodegeneration", *Glia*, vol. 65, no. 12, pp. 1885–1899, 2017.

[40] Y. Wang, A. Narayanaswamy, C.-L. Tsai, and B. Roysam, "A broadly applicable 3-d neuron tracing method based on open-curve snake", *Neuroinformatics*, vol. 9, no. 2-3, pp. 193–217, 2011.

[41] Y. Wang, A. Narayanaswamy, and B. Roysam, "Novel 4-d open-curve active contour and curve completion approach for automated tree structure extraction", in *CVPR 2011*, IEEE, 2011, pp. 1105–1112.

[42] S. Yona, K.-W. Kim, Y. Wolf, A. Mildner, D. Varol, M. Breker, D. Strauss-Ayali, S. Viukov, M. Guilliams, A. Misharin, *et al.*, "Fate mapping reveals origins and dynamics of monocytes and tissue macrophages under homeostasis", *Immunity*, vol. 38, no. 1, pp. 79–91, 2013.

[43] L. Madisen, T. A. Zwingman, S. M. Sunkin, S. W. Oh, H. A. Zariwala, H. Gu, L. L. Ng, R. D. Palmiter, M. J. Hawrylycz, A. R. Jones, *et al.*, "A robust and high-throughput cre reporting and characterization system for the whole mouse brain", *Nature Neuroscience*, vol. 13, no. 1, p. 133, 2010.

[44] S. T. Acton and N. Ray, "Biomedical image analysis: Segmentation", *Synthesis Lectures on Image, Video, and Multimedia Processing*, vol. 4, no. 1, pp. 1–108, 2009.

[45] S. Mukherjee, B. Condron, and S. T. Acton, "Tubularity flow field — a technique for automatic neuron segmentation", *IEEE Transactions on Image Processing*, vol. 24, no. 1, pp. 374–389, 2015.

[46] M. Kass, A. Witkin, and D. Terzopoulos, "Snakes: Active contour models", *International Journal of Computer Vision*, vol. 1, no. 4, pp. 321–331, 1988.

[47] R. Malladi, J. A. Sethian, and B. C. Vemuri, "Shape modeling with front propagation: A level set approach", *IEEE Transactions on Pattern Analysis and Machine Intelligence*, vol. 17, no. 2, pp. 158–175, 1995.

[48] B. Li and S. T. Acton, "Active contour external force using vector field convolution for image segmentation", *IEEE transactions on image processing*, vol. 16, no. 8, pp. 2096–2106, 2007.

[49] A.-R. Mansouri, D. P. Mukherjee, and S. T. Acton, "Constraining active contour evolution via lie groups of transformation", *IEEE Transactions on Image Processing*, vol. 13, no. 6, pp. 853–863, 2004.

[50] N. Ray and S. T. Acton, "Active contours for cell tracking", in *Image Analysis and Interpretation, 2002. Proceedings. Fifth IEEE Southwest Symposium on*, IEEE, 2002, pp. 274–278.

[51] A. P. Goobic, J. Tang, and S. T. Acton, "Image stabilization and registration for tracking cells in the microvasculature", *IEEE Transactions on Biomedical Engineering*, vol. 52, no. 2, pp. 287–299, 2005.

[52] J. Cui, S. T. Acton, and Z. Lin, "A monte carlo approach to rolling leukocyte tracking in vivo", *Medical Image Analysis*, vol. 10, no. 4, pp. 598–610, 2006.

[53] A. F. Frangi, W. J. Niessen, K. L. Vincken, and M. A. Viergever, "Multiscale vessel enhancement filtering", in *International Conference on Medical Image Computing and Computer-Assisted Intervention*, Springer, 1998, pp. 130–137.

[54] L. Antiga, "Generalizing vesselness with respect to dimensionality and shape", *The Insight Journal*, vol. 3, pp. 1–14, 2007.

[55] S. Mukherjee and S. T. Acton, "Region based segmentation in presence of intensity inhomogeneity using legendre polynomials", *IEEE Signal Processing Letters*, vol. 22, no. 3, pp. 298–302, 2015.

[56] T. F. Chan and L. A. Vese, "Active contours without edges", *IEEE Transactions on Image Processing*, vol. 10, no. 2, pp. 266–277, 2001.

[57] P. K. Saha, G. Borgefors, and G. S. di Baja, *Skeletonization: Theory, methods and applications*. Academic Press, 2017.

[58] Y. Xiong, C. Kabacoff, J. Franca-Koh, P. N. Devreotes, D. N. Robinson, and P. A. Iglesias, "Automated characterization of cell shape changes during amoeboid motility by skeletonization", *BMC systems biology*, vol. 4, no. 1, pp. 1–18, 2010.

[59] L. Verscheure, L. Peyrodie, A.-S. Dewalle, N. Reyns, N. Betrouni, S. Mordon, and M. Vermandel, "Three-dimensional skeletonization and symbolic description in vascular imaging: Preliminary results", *International journal of computer assisted radiology and surgery*, vol. 8, no. 2, pp. 233–246, 2013.

[60] Y. Chen, K. Drechsler, W. Zhao, and C. O. Laura, "A thinning-based liver vessel skeletonization method", in *2011 International Conference on Internet Computing and Information Services*, IEEE, 2011, pp. 152–155.

[61] M. Ahmed and R. Ward, "A rotation invariant rule-based thinning algorithm for character recognition", *IEEE Transactions on Pattern Analysis and Machine Intelligence*, vol. 24, no. 12, pp. 1672–1678, 2002.

[62] H. Blum *et al.*, *A transformation for extracting new descriptors of shape*. MIT press Cambridge, 1967, vol. 4.

[63] S. Mukherjee, S. Basu, B. Condron, and S. T. Acton, "Tree2tree2: Neuron tracing in 3d", in *Biomedical Imaging (ISBI), 2013 IEEE 10th International Symposium on*, IEEE, 2013, pp. 448–451.

[64] H. Peng, Z. Ruan, D. Atasoy, and S. Sternson, "Automatic reconstruction of 3d neuron structures using a graph-augmented deformable model", *Bioinformatics*, vol. 26, no. 12, pp. i38–i46, 2010.

[65] E. W. Dijkstra, "A note on two problems in connexion with graphs", *Numerische mathematik*, vol. 1, no. 1, pp. 269–271, 1959.

[66] P. Kollmannsberger, M. Kerschnitzki, F. Repp, W. Wagermaier, R. Weinkamer, and P. Fratzl, "The small world of osteocytes: Connectomics of the lacuno-canalicular network in bone", *New Journal of Physics*, vol. 19, no. 7, p. 073 019, 2017.

[67] Y. Sato, S. Nakajima, N. Shiraga, H. Atsumi, S. Yoshida, T. Koller, G. Gerig, and R. Kikinis, "Three-dimensional multi-scale line filter for segmentation and visualization of curvilinear structures in medical images", *Medical image analysis*, vol. 2, no. 2, pp. 143–168, 1998.

[68] T. Ly, J. Thompson, T. Harris, and S. T. Acton, "The coupled tuff-bff algorithm for automatic 3d segmentation of microglia", pp. 121–125, 2018.

[69] T.-C. Lee, R. L. Kashyap, and C.-N. Chu, "Building skeleton models via 3-d medial surface axis thinning algorithms", *CVGIP: Graphical Models and Image Processing*, vol. 56, no. 6, pp. 462–478, 1994.

[70] H. Homann, "Implementation of a 3d thinning algorithm", *Insight Journal*, vol. 421, 2007.

[71] M. H. Longair, D. A. Baker, and J. D. Armstrong, "Simple neurite tracer: Open source software for reconstruction, visualization and analysis of neuronal processes", *Bioinformatics*, vol. 27, no. 17, pp. 2453–2454, 2011.

[72] S. Osher and J. A. Sethian, "Fronts propagating with curvature-dependent speed: Algorithms based on hamilton-jacobi formulations", *Journal of computational physics*, vol. 79, no. 1, pp. 12–49, 1988.

[73] C. Xu and J. L. Prince, "Snakes, shapes, and gradient vector flow", *IEEE Transactions on image processing*, vol. 7, no. 3, pp. 359–369, 1998.

[74] S. Mukherjee and S. T. Acton, "Vector field convolution medialness applied to neuron tracing", in *2013 IEEE International Conference on Image Processing*, IEEE, 2013, pp. 665–669.

[75] S. Basu, A. Aksel, B. Condron, and S. T. Acton, "Segmentation and tracing of neurons in 3d", *IEEE Transactions on Info. Tech. Biomedicine*, 2012.

[76] Z. Xiao, J. Ni, Q. Liu, L. Jiang, and X. Wang, "Study on automatic tracking algorithm of neurons in most atlas of mouse brain based on open curve snake", in *2017 IEEE 4th International Conference on Soft Computing & Machine Intelligence (ISCMI)*, IEEE, 2017, pp. 140–144.

[77] D. Sui, K. Wang, Y. Zhang, and H. Zhang, "A novel seeding method based on spatial sliding volume filter for neuron reconstruction", in *2013 IEEE International Conference on Bioinformatics and Biomedicine*, IEEE, 2013, pp. 29–34.

[78] D. Sui, K. Wang, J. Chae, Y. Zhang, and H. Zhang, "A pipeline for neuron reconstruction based on spatial sliding volume filter seeding", *Computational and mathematical methods in medicine*, vol. 2014, 2014.

[79] D. Jan-Kroon, *Comprehensive meta-analysis*, Hessian based Frangi Vesselness Filter, 2021.

[80] M. S. Hassouna and A. A. Farag, "Multistencils fast marching methods: A highly accurate solution to the eikonal equation on cartesian domains", *IEEE transactions on pattern analysis and machine intelligence*, vol. 29, no. 9, pp. 1563–1574, 2007.

[81] H. Xiao and H. Peng, "App2: Automatic tracing of 3d neuron morphology based on hierarchical pruning of a gray-weighted image distance-tree", *Bioinformatics*, vol. 29, no. 11, pp. 1448–1454, 2013.

[82] J. Yang, M. Hao, X. Liu, Z. Wan, N. Zhong, and H. Peng, "Fmst: An automatic neuron tracing method based on fast marching and minimum spanning tree", *Neuroinformatics*, vol. 17, no. 2, pp. 185–196, 2019.

[83] J. Xie, T. Zhao, T. Lee, E. Myers, and H. Peng, "Anisotropic path searching for automatic neuron reconstruction", *Medical image analysis*, vol. 15, no. 5, pp. 680–689, 2011.

[84] H. Peng, Z. Ruan, F. Long, J. H. Simpson, and E. W. Myers, "V3d enables real-time 3d visualization and quantitative analysis of large-scale biological image data sets", *Nature biotechnology*, vol. 28, no. 4, pp. 348–353, 2010.

[85] A. M. Fontainhas, M. Wang, K. J. Liang, S. Chen, P. Mettu, M. Damani, R. N. Fariss, W. Li, and W. T. Wong, "Microglial morphology and dynamic behavior is regulated by ionotropic glutamatergic and gabaergic neurotransmission", *PloS one*, vol. 6, no. 1, e15973, 2011.

[86] A. G. Orr, A. L. Orr, X.-J. Li, R. E. Gross, and S. F. Traynelis, "Adenosine a 2a receptor mediates microglial process retraction", *Nature neuroscience*, vol. 12, no. 7, p. 872, 2009.

[87] N. Stence, M. Waite, and M. E. Dailey, "Dynamics of microglial activation: A confocal time-lapse analysis in hippocampal slices", *Glia*, vol. 33, no. 3, pp. 256–266, 2001.

[88] M. d. M. Fernández-Arjona, J. M. Grondona, P. Granados-Durán, P. Fernández-Llebrez, and M. D. López-Ávalos, "Microglia morphological categorization in a rat model of neuroinflammation by hierarchical cluster and principal components analysis", *Frontiers in cellular neuroscience*, vol. 11, p. 235, 2017.

[89] D. A. Sholl, "Dendritic organization in the neurons of the visual and motor cortices of the cat", *Journal of anatomy*, vol. 87, no. Pt 4, p. 387, 1953.

[90] A. M. Reeves, E. Shigetomi, and B. S. Khakh, "Bulk loading of calcium indicator dyes to study astrocyte physiology: Key limitations and improvements using morphological maps", *Journal of Neuroscience*, vol. 31, no. 25, pp. 9353–9358, 2011.

[91] J. Schoenen, "The dendritic organization of the human spinal cord: The dorsal horn", *Neuroscience*, vol. 7, no. 9, pp. 2057–2087, 1982.

[92] T. Batabyal and S. T. Acton, "Elastic path2path: Automated morphological classification of neurons by elastic path matching", in *2018 25th ieee international conference on image processing (icip)*, IEEE, 2018, pp. 166–170.

[93] T. T. Ly, T. Batabyal, J. Thompson, T. Harris, D. S. Weller, and S. T. Acton, "Hieroglyph: Hierarchical glia graph skeletonization and matching", *Asilomar Conference on Signals, Systems and Computers*, 2020.

[94] S. Basu, B. Condron, and S. T. Acton, "Path2path: Hierarchical path-based analysis for neuron matching", in *2011 ieee international symposium on biomedical imaging: From nano to macro*, IEEE, 2011, pp. 996–999.

[95] R. M. Bryan and D. Attwell, "Microglial ramification, surveillance, and interleukin-1b release are regulated by the two-pore domain k channel thik-1", *Neuron*, vol. 97, pp. 1–14, 2018.